The Astrophysical Journal, 974:192 (26pp), 2024 October 20 https://doi.org/10.3847/1538-4357/ad6b94

J-PLUS: Beyond Spectroscopy. III. Stellar Parameters and Elemental-abundance Ratios for Five Million Stars from DR3

Yang Huang (黄样)[1,2,3], Timothy C. Beers[4], Kai Xiao (肖凯)[1], Haibo Yuan (苑海波)[3,5], Young Sun Lee[4,6], Hongrui Gu (顾弘睿)[1,2], Jihye Hong[4], Jifeng Liu (刘继峰)[2,1,3], Zhou Fan (范舟)[1,2], Paula Coelho[7], Patricia Cruz[8], F. J. Galindo-Guil[9], Simone Daflon[10], Fran Jiménez-Esteban[8], Javier Cenarro[11], David Cristóbal-Hornillos[11], Carlos Hernández-Monteagudo[12], Carlos López-Sanjuan[11], Antonio Marín-Franch[11], Mariano Moles[11], Jesús Varela[11], Héctor Vázquez Ramió[11], Jailson Alcaniz[10], Renato Dupke[10], Alessandro Ederoclite[11], Laerte Sodré, Jr.[7], and Raul E. Angulo[13]
[1] School of Astronomy and Space Science, University of Chinese Academy of Sciences, Beijing 100049, People's Republic of China; huangyang@ucas.ac.cn
[2] CAS Key Lab of Optical Astronomy, National Astronomical Observatories, Chinese Academy of Sciences, Beijing 100012, People's Republic of China
[3] Institute for Frontiers in Astronomy and Astrophysics, Beijing Normal University, Beijing 102206, People's Republic of China
[4] Department of Physics and Astronomy and JINA Center for the Evolution of the Elements (JINA-CEE), University of Notre Dame, Notre Dame, IN 46556, USA
[5] Department of Astronomy, Beijing Normal University, Beijing 100875, People's Republic of China
[6] Department of Astronomy and Space Science, Chungnam National University, Daejeon 34134, Republic of Korea
[7] Universidade de São Paulo, Instituto de Astronomia, Geofísica e Ciências Atmosféricas, Rua do Matão 1226, São Paulo, 05508-090, SP, Brazil
[8] Centro de Astrobiología, CSIC-INTA, Camino Bajo del Castillo s/n, E-28692, Villanueva de la Cañada, Madrid, Spain
[9] Centro de Estudios de Física del Cosmos de Aragón (CEFCA), Plaza San Juan 1, 44001, Teruel, Spain
[10] Observatório Nacional, Rua Gal. José Cristino 77, Rio de Janeiro, 20921-400, RJ, Brazil
[11] Centro de Estudios de Física del Cosmos de Aragón (CEFCA), Unidad Asociada al CSIC, Plaza San Juan 1, 44001, Teruel, Spain
[12] Instituto de Astrofísica de Canarias (IAC), C/Vía Láctea, S/N, E-38205, La Laguna, Tenerife, Spain
[13] Donostia International Physics Center, Paseo Manuel de Lardizabal 4, 20018, Donostia-San Sebastián, Spain
Received 2023 November 27; revised 2024 August 3; accepted 2024 August 4; published 2024 October 11

Abstract

We present a catalog of stellar parameters (effective temperature $T_{\rm eff}$, surface gravity $\log g$, age, and metallicity [Fe/H]) and elemental-abundance ratios ([C/Fe], [Mg/Fe], and [α/Fe]) for some five million stars (4.5 million dwarfs and 0.5 million giant stars) in the Milky Way, based on stellar colors from the Javalambre Photometric Local Universe Survey (J-PLUS) DR3 and Gaia EDR3. These estimates are obtained through the construction of a large spectroscopic training set with parameters and abundances adjusted to uniform scales, and trained with a kernel principal component analysis. Owing to the seven narrow/medium-band filters employed by J-PLUS, we obtain precisions in the abundance estimates that are as good as or better than those derived from medium-resolution spectroscopy for stars covering a wide range of the parameter space: 0.10–0.20 dex for [Fe/H] and [C/Fe], and 0.05 dex for [Mg/Fe] and [α/Fe]. Moreover, systematic errors due to the influence of molecular carbon bands on previous photometric-metallicity estimates (which only included two narrow/medium-band blue filters) have now been removed, resulting in photometric-metallicity estimates down to [Fe/H] ~ -4.0, with typical uncertainties of 0.40 dex and 0.25 dex for dwarfs and giants, respectively. This large photometric sample should prove useful for the exploration of the assembly and chemical-evolution history of our Galaxy.

Unified Astronomy Thesaurus concepts: Galaxy stellar content (621); Fundamental parameters of stars (555); Stellar distance (1595); Astronomy data analysis (1858)

1. Introduction

Over the past decade, great advances have been achieved in the field of Galactic archeology due to the determinations of precise stellar parameters and individual elemental-abundance ratios for large numbers of stars obtained by massive spectroscopic surveys, such as the Sloan Digital Sky Survey (SDSS; York et al. 2000), the RAVE survey (Steinmetz et al. 2006), the SDSS/SEGUE survey (Yanny et al. 2009; Rockosi et al. 2022), the GALAH survey (De Silva et al. 2015), the SDSS/APOGEE survey (Majewski et al. 2017), the LAMOST survey (Deng et al. 2012; Zhao et al. 2012), and the Gaia-ESO survey (Gilmore et al. 2022; Randich et al. 2022). In the era of Gaia, accurate 3D positions and proper motions are now available for billions of stars. However, despite these extensive efforts, the number of stars with spectroscopic information lags far behind those with full astrometric information, by at least two orders of magnitude, leading to a limited and potentially biased view of the stellar populations in the Milky Way (MW).

In order to alleviate this mismatch between the numbers of stars with available spectroscopic and astrometric information, we have pursued approaches to obtain estimates of stellar parameters (and a limited number of other important elemental-abundance ratios) through the use of ongoing or planned narrow/medium-bandwidth photometric surveys (see the summary in Table 1 of Huang et al. 2022). In the first two papers of this series (Huang et al. 2022, 2023, hereafter Papers I and II), stellar parameters, in particular the metallicity, are derived for nearly 50 million stars covering around 3π sr of the sky, using *uv* narrowband photometric data obtained from the SAGES DR1 catalog of the northern sky (Fan et al. 2023) and the SkyMapper catalog in the southern sky (SMSS; Wolf et al. 2018; Onken et al. 2019), combined with Gaia EDR3 broadband photometry and astrometric information (Gaia Collaboration et al. 2021). The huge numbers of stars and deep limiting magnitudes of the derived parameter catalogs are

poised to revolutionize our knowledge of the MW, and also serve to identify stars of particular interest for detailed study at high spectral resolution.

Building on our efforts with SAGES and SkyMapper, we now take the next step forward, measuring not only [Fe/H], but also other elemental-abundance ratios (including the most important ratios for analyses of stellar populations—[C/Fe], [Mg/Fe], and [α/Fe][14]), based on the filter fluxes from the publicly available third data release of the Javalambre Photometric Local Universe Survey (J-PLUS DR3).[15] The 12 filters employed by J-PLUS include seven narrow/medium-band filters (with FHWM from 100 to 400 Å; J0378, J0395, J0410, J0430, J0515, J0660, J0861), designed to detect prominent stellar absorption features (including the Ca II H + K lines, the molecular CH *G*-band, Hδ, the Mg b triplet, Hα, and the Ca I triplet), along with five SDSS-like broadband filters (*ugriz*).

The construction of training sets is of crucial importance to calibrate estimates of the stellar parameters and elemental-abundance ratios from photometric colors. We have thus assembled a large database of several million stars with spectroscopically derived stellar parameters from a number of surveys, carefully calibrated to uniform scales, as described in this paper.

This paper is structured as follows. Section 2 introduces the main data used in this work. Section 3 describes the construction of training sets, including the calibrations of the individual parameter scales. Estimates of stellar parameters and elemental-abundance ratios are presented in Section 4. Section 5 describes our estimates of effective temperatures, distances, ages, and surface gravities. Section 6 describes our final sample. Section 7 provides a summary and future prospects.

2. Data

2.1. J-PLUS DR3

J-PLUS (Cenarro et al. 2019) is an ongoing survey aimed at observing about 8500 deg^2 of the sky visible from the Observatorio Astrofísico de Javalambre (OAJ; Cenarro et al. 2014), using the JAST80 telescope equipped with the panoramic camera T80Cam (2 deg^2 field of view provided by a single CCD of 9.2k × 9.2k pixels). This survey adopted 12 specially designed narrowband, medium-band, and broadband optical filters; their properties are summarized in Table 1. J-PLUS observations are mainly made under seeing conditions better than 1.″5 and airmass smaller than 1.5. Here we use the data from the third public data release, J-PLUS DR3, which covers 3192 deg^2 (1642 fields) for all 12 bands, with an *r*-band limiting magnitude down to 21.8 (5σ, 3″ diameter aperture). In total, about 47.4 million sources are released in the J-PLUS DR3 catalog. The photometric observations were initially calibrated using Gaia BP/RP (XP) ultralow-resolution spectra (López-Sanjuan et al. 2024). Significant improvements in the zero-points of the filter photometry have been been made through recalibration using the stellar color regression method and an improved Gaia XP synthetic photometry method (Xiao et al. 2024); the final accuracy of the zero-points in the photometric calibrations is 1–5 mmag.

Table 1
Summary of the J-PLUS Filter System

Filter	$\lambda_{\rm eff}$ (Å)	FWHM (Å)	$k_\chi = \frac{A_\chi}{E(B-V)}$	Comments
u	3485	508	4.479	Balmer-break region
J0378	3785	168	4.294	O II
J0395	3950	100	4.226	Ca H + K
J0410	4100	200	4.023	Hδ
J0430	4300	200	3.859	CH *G*-band
g	4803	1409	3.398	SDSS
J0515	5150	200	3.148	Mg b triplet
r	6254	1388	2.383	SDSS
J0660	6600	138	2.161	Hα
i	7668	1535	1.743	SDSS
J0861	8610	400	1.381	Ca triplet
z	9114	1409	1.289	SDSS

2.2. Gaia EDR3

In addition to J-PLUS DR3, Gaia EDR3 broadband photometry (*G*, $G_{\rm BP}$, and $G_{\rm RP}$) is also used in this study. In Gaia EDR3 (Gaia Collaboration et al. 2021), the broadband photometry, as well as astrometric information (parallaxes and proper motions), is provided for about 1.5 billion sources with magnitudes down to $G \sim 21$, although the completeness is quite complicated at the faint end (see details in Riello et al. 2021). The photometric uncertainty is only a few millimagnitudes for the *G*-band photometry even at $G = 20$, around 10 mmag for $G_{\rm BP}$ and $G_{\rm RP}$ at $G = 17$, and no worse than 100 mmag for $G_{\rm BP}$ and $G_{\rm RP}$ at $G = 20$.

By cross-matching J-PLUS DR3 with Gaia EDR3 and requiring $r \leqslant 21.0$ and *class_star* $\geqslant 0.6$, yielded by `SExtractor` (Bertin & Arnouts 1996), over 16.5 million stars are left from the original J-PLUS DR3 sample. This sample is adopted in the following analysis. In this study, the extinction map of Schlegel et al. (1998, hereafter the SFD map[16]) is adopted for reddening corrections, since over 90% of the J-PLUS DR3 stars are located at higher Galactic latitudes ($|b| \geqslant 15°$). The reddening coefficients ($k_\chi = \frac{A_\chi}{E(B-V)}$, see Table 1) for the J-PLUS and Gaia EDR3 photometric passbands are empirically estimated in López-Sanjuan et al. (2021) and Huang et al. (2021), respectively, using the star-pair technique described by Yuan et al. (2013).

2.3. Spectroscopic Surveys

External estimates of the stellar parameters ($T_{\rm eff}$, log *g*, and [Fe/H]) are adopted from a master catalog assembled from completed/ongoing large-scale spectroscopic surveys, including the SDSS/SEGUE, LAMOST, SDSS/APOGEE, and GALAH surveys.

The SDSS/SEGUE stellar parameters for hundreds of thousands of stars are those released in SDSS DR12 (Alam et al. 2015), based on low-resolution ($R \sim 2000$) optical spectra collected by the 2.5 m Sloan Foundation Telescope at Apache Point Observatory (APO; Gunn et al. 2006). The stellar

[14] [α/Fe] is the total α-element abundance relative to iron, and is influenced by a combination of all α-elements. In APOGEE, it is mainly determined by O, Mg, S, Si, Ca, and Ti. In GALAH, it is mainly determined by O, Ne, Mg, Si, S, Ar, Ca, and Ti.

[15] https://archive.cefca.es/catalogs/jplus-dr3

[16] Note that the overestimated 14% systematic offset in extinction is corrected for.

parameters are derived using the SEGUE Stellar Parameter Pipeline (SSPP; Lee et al. 2008). The typical metallicity uncertainty is around 0.15 dex.

Nearly five million stars with precise metallicity estimates, as well as other stellar parameters, are adopted from DR9[17] of LAMOST, a 4 m quasi-meridian reflecting Schmidt telescope equipped with 4000 fibers distributed over a field of view of 5° in diameter (Cui et al. 2012); these parameters are estimated from SDSS-like low-resolution ($R \sim 2000$) optical spectra by using the LAMOST Stellar Parameter Pipeline (LASP; Luo et al. 2015). The metallicity uncertainty is 0.10–0.15 dex.

The latest SDSS DR17 (Abdurro'uf et al. 2022) has released atmospheric parameters and over 20 elemental-abundance ratios for over 600,000 stars based on near-infrared (H band; 1.51–1.70 μm) high-resolution ($R \sim 22{,}500$) spectra collected by the APOGEE-1 and APOGEE-2 surveys (Majewski et al. 2017). These spectra are obtained by the 2.5 m Sloan Foundation Telescope (Gunn et al. 2006) at APO in the Northern Hemisphere, and the 2.5 m Irénée du Pont Telescope (Bowen & Vaughan 1973) at Las Campanas Observatory in the Southern Hemisphere. The uncertainties in [Fe/H] and for the elemental-abundance ratios we employ in this study ([C/Fe], [Mg/Fe], and [α/Fe]) are 0.10 dex, 0.02 dex, and 0.02 dex, respectively.

The GALAH survey is a large optical high-resolution ($R \sim 28{,}000$) spectroscopic survey using the HERMES spectrograph installed on the 3.9 m Anglo-Australian Telescope (De Silva et al. 2015). GALAH DR3 has released metallicity estimates and up to 30 elemental-abundance ratios for over 0.5 million stars (Buder et al. 2021); the typical uncertainties of the [Fe/H] estimates are better than 0.10 dex, and the pertinent elemental-abundance ratios are precise to better than 0.02–0.03 dex.

3. Training Sets and Derivation of Uniform Parameter Scales

In this section, we describe the training sets we employ for obtaining estimates of the metallicity ([Fe/H]) and elemental abundances ([C/Fe], [Mg/Fe], [α/Fe]) measured by previous spectroscopic surveys. We emphasize that this effort is not only important for the current study, but also can be adopted by future work on estimating stellar parameters either from multiple colors or from spectroscopy.

3.1. Metallicity ([Fe/H])

We adopted metallicity measurements ([Fe/H]) based on high-resolution spectroscopy (HRS) as the reference scale, merging measurements from the Stellar Abundances for Galactic Archaeology (SAGA) Database (Suda et al. 2008) and the PASTEL catalog (Soubiran et al. 2016).

For stars with multiple measurements, the average values are adopted. As evaluated in Figure 1 of Paper I, the accuracy is better than 0.05 dex for stars with [Fe/H] > -2.0 and 0.05–0.10 dex for stars with [Fe/H] $\leqslant -2.0$. The metallicity scale of our compiled sample is compared to the largest homogeneous sample of 400 very metal-poor stars collected by Subaru Telescope (Li et al. 2022, see Figure A3). From inspection, they are very consistent with each other, with small mean residuals and a scatter of 0.17 dex. In total, 24,160 stars

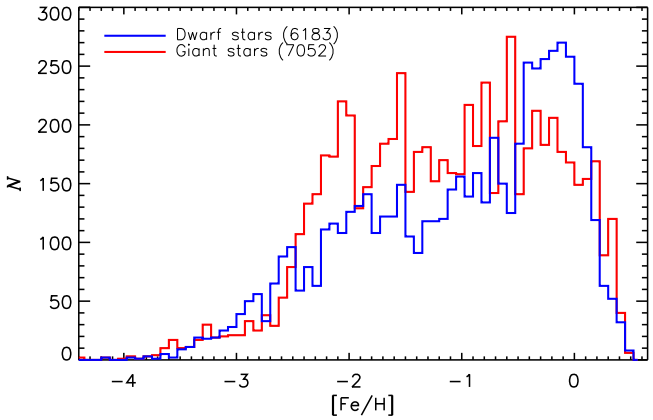

Figure 1. Histograms of the training sets for metallicity ([Fe/H]) for dwarfs (blue line) and giants (red line).

with [Fe/H] between −5.7 and +1.0 form the HRS database as the reference scale (see Table A1).

The metallicity estimated from the completed/ongoing spectroscopic surveys is then compared to the HRS sample (Figure A1). Generally, the metal-rich stars ([Fe/H] > -1.5) of SDSS/APOGEE, GALAH, and SDSS/SEGUE surveys are consistent with those of the HRS sample, while the metal-poor regions ([Fe/H] $\leqslant -1.5$) deviate from the HRS metallicity scale and exhibit a larger scatter.

To correct for the deviations, second- to third-order polynomials are adopted with the coefficients marked in Figure A1. The revised APOGEE metallicity is then adopted to calibrate the stellar parameters from LAMOST in the $T_{\rm eff}$, $\log g$, and [Fe/H] spaces (Figure A2), given the large number of stars in common. As shown in Figures A1 and A2, most of the usual survey pipelines[18] are only able to derive metallicity down to [Fe/H] $= -2.5$, and not much more metal-poor than [Fe/H] $= -3.0$, from the existing spectroscopic surveys. To improve the calibration at the metal-poor end, we adopted a custom version of the SSPP (the LSSPP; Lee et al. 2015) for the LAMOST spectra, and the latest version of the SSPP for the SDSS/SEGUE spectra, in order to derive metallicities for hundreds of thousands of metal-poor stars (down to [Fe/H] $=$ -4.0) from both surveys.

All of the spectra for those metal-poor stars were visually inspected (by Beers), and any problematic spectra (e.g., defects that might compromise their determinations, as well as contamination from cool white dwarfs, hot B-type subdwarf stars, and emission-line objects) are excluded. The comparisons show that the LSSPP/SSPP metallicity is consistent with that of the HRS scale (see Figure A3), even at the metal-poor end ([Fe/H] ~ -4.0), with no significant offset and a typical scatter of 0.20–0.30 dex.

The HRS, SDSS/APOGEE, LAMOST, and LAMOST +SEGUE very metal-poor (VMP; [Fe/H] $\leqslant -2.0$) samples are then cross-matched with the J-PLUS parent sample to build up the training sample at low metallicity. The SDSS/SEGUE and GALAH sample stars are then used for validation purposes.

When constructing the training set, the stars are required to satisfy the following criteria: (1) photometric uncertainties

[17] http://www.lamost.org/dr9/v1.1/

[18] For example, the LASP by Luo et al. (2015) and the APOGEE Stellar Parameter and Chemical Abundances Pipeline (ASPCAP) by García Pérez et al. (2016).

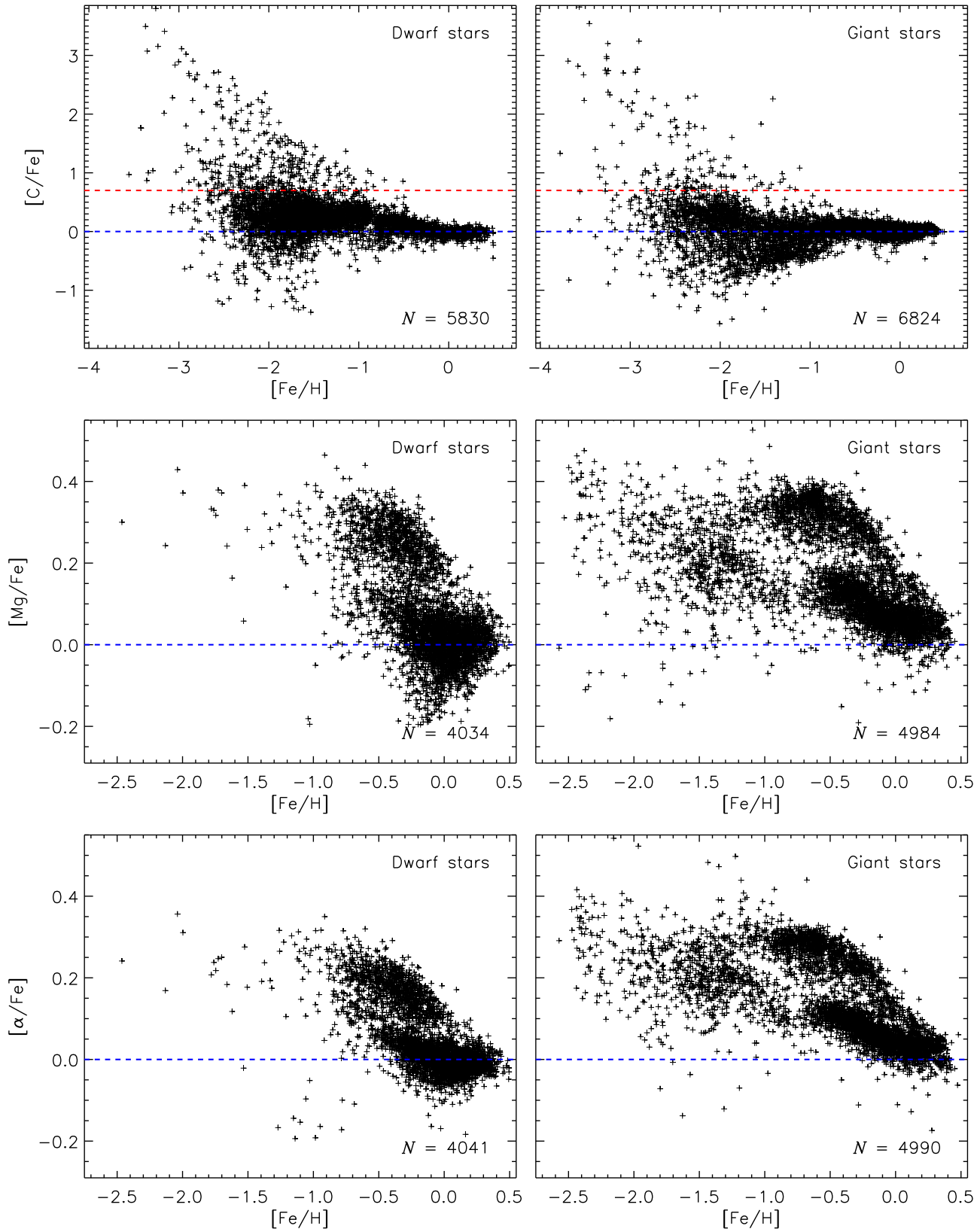

Figure 2. Distributions of stars in the training sample for [C/Fe] in the [C/Fe] vs. [Fe/H] space (top panels), for [Mg/Fe] in the [Mg/Fe] vs. [Fe/H] space (middle panels), and for [α/Fe] in the [α/Fe] vs. [Fe/H] space (bottom panels). The left column is for dwarf stars and the right column is for giant stars. The red dashed lines in the top panels mark the [C/Fe] value of +0.7, the criterion often used to define CEMP stars. Note that for our present purpose, we report the measured estimate of [C/Fe], without applying evolutionary corrections. The blue dashed lines in each panel indicate the solar ratios.

smaller than 0.04 mag in the 12 J-PLUS bands, and 0.02 mag in the three Gaia bands; (2) higher Galactic latitudes ($|b| \geqslant 15°$) and low extinction values ($E(B-V) \leqslant 0.04$); and (3) metallicities estimated from high-quality spectra with signal-to-noise ratio (SNR) at least 20 pixel^{-1}. The stars in the training sample are further divided into dwarfs and giants according to

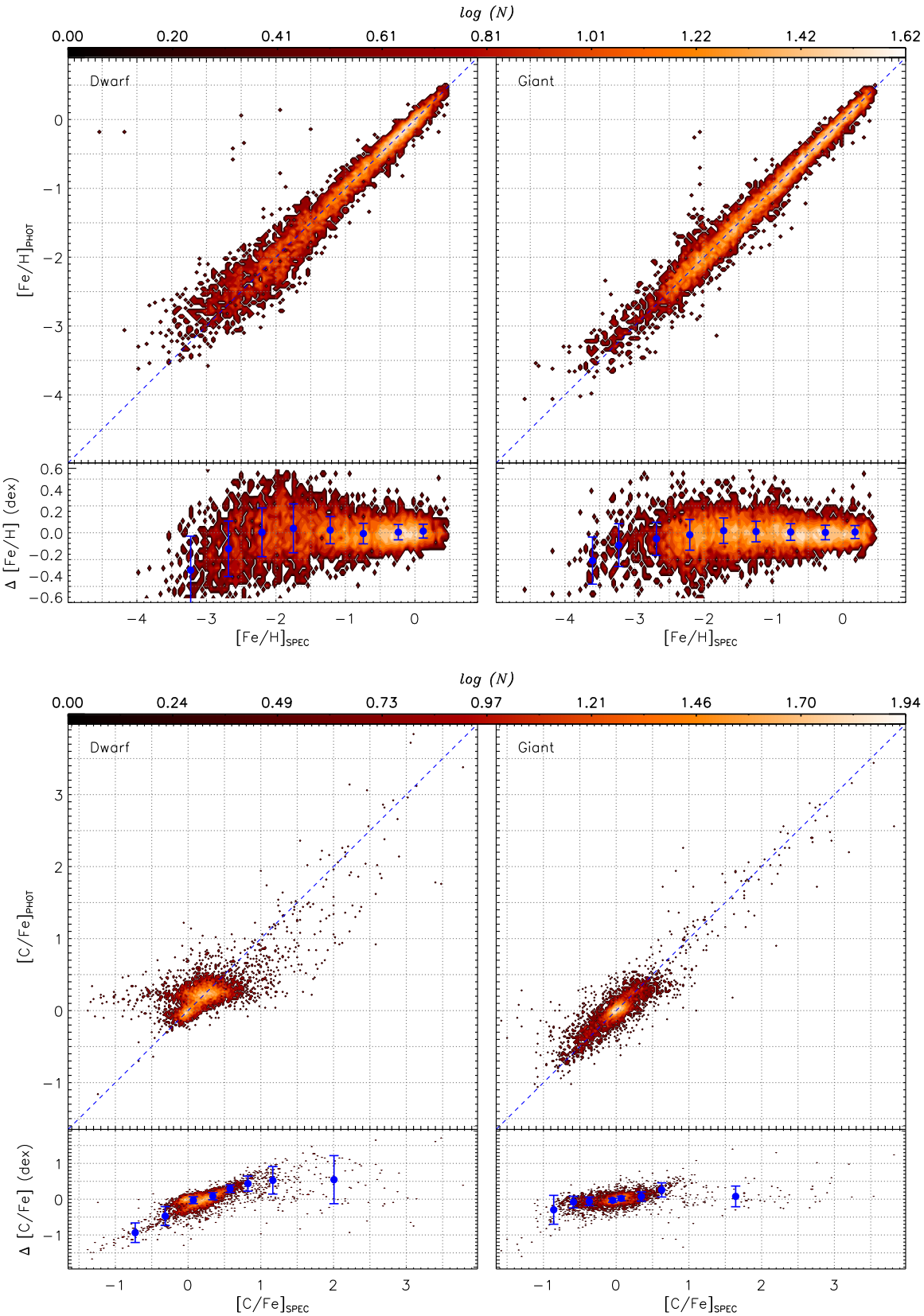

Figure 3. Comparisons between the photometric and spectroscopic metallicities (top panels) and the photometric and spectroscopic [C/Fe] (bottom panels) for the dwarf stars (left column) and giant stars (right column) in the training sample. The photometric results are estimated from the multiple colors formed with the combination of the J-PLUS DR3 and Gaia EDR3 magnitudes using a KPCA technique (see text). The lower part of each panel shows the parameter differences (photometric minus spectroscopic) as a function of the spectroscopic determinations. The blue dots and error bars in each panel represent the median and dispersion of the parameter differences in the individual parameter bins. The blue dashed lines are the one-to-one lines. A color bar representing the numbers of stars is provided at the top of each set of panels.

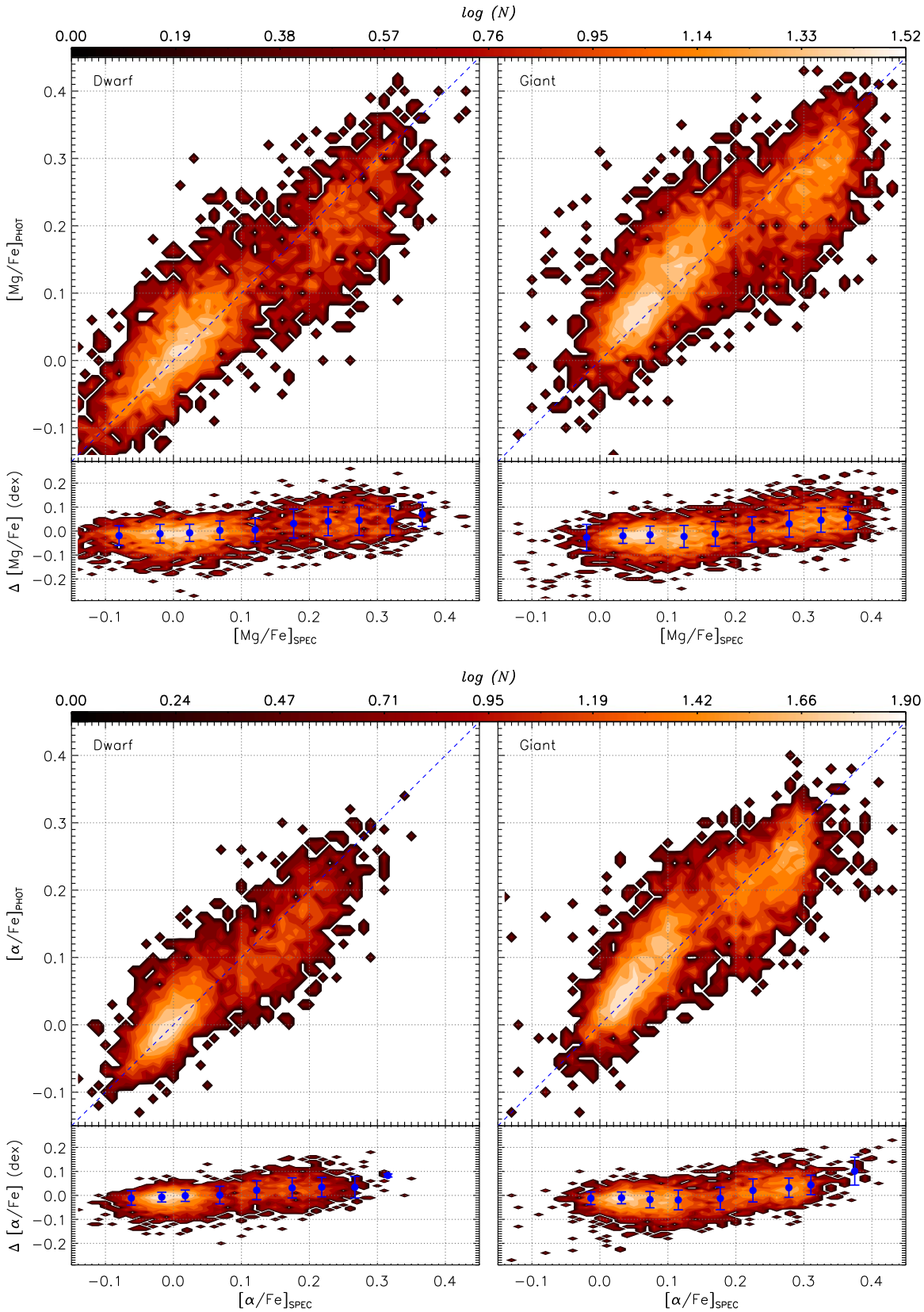

Figure 4. Similar to Figure 3, but for [Mg/Fe] (top panels) and [α/Fe] (bottom panels).

an empirical cut in the $(G_{\rm BP} - G_{\rm RP})_0$–$M_G$ diagram (see Paper I); the G-band absolute magnitudes are derived from Gaia G (extinction corrected), and geometric distances are estimated from Bayesian-based Gaia parallax measurements (Bailer-Jones et al. 2021). All of the metal-poor stars ([Fe/H] $\leqslant -2.0$) that satisfy the above criteria are selected. To achieve good training results for the entire metallicity range, a similar number of relatively more metal-rich ([Fe/H] > -2.0)

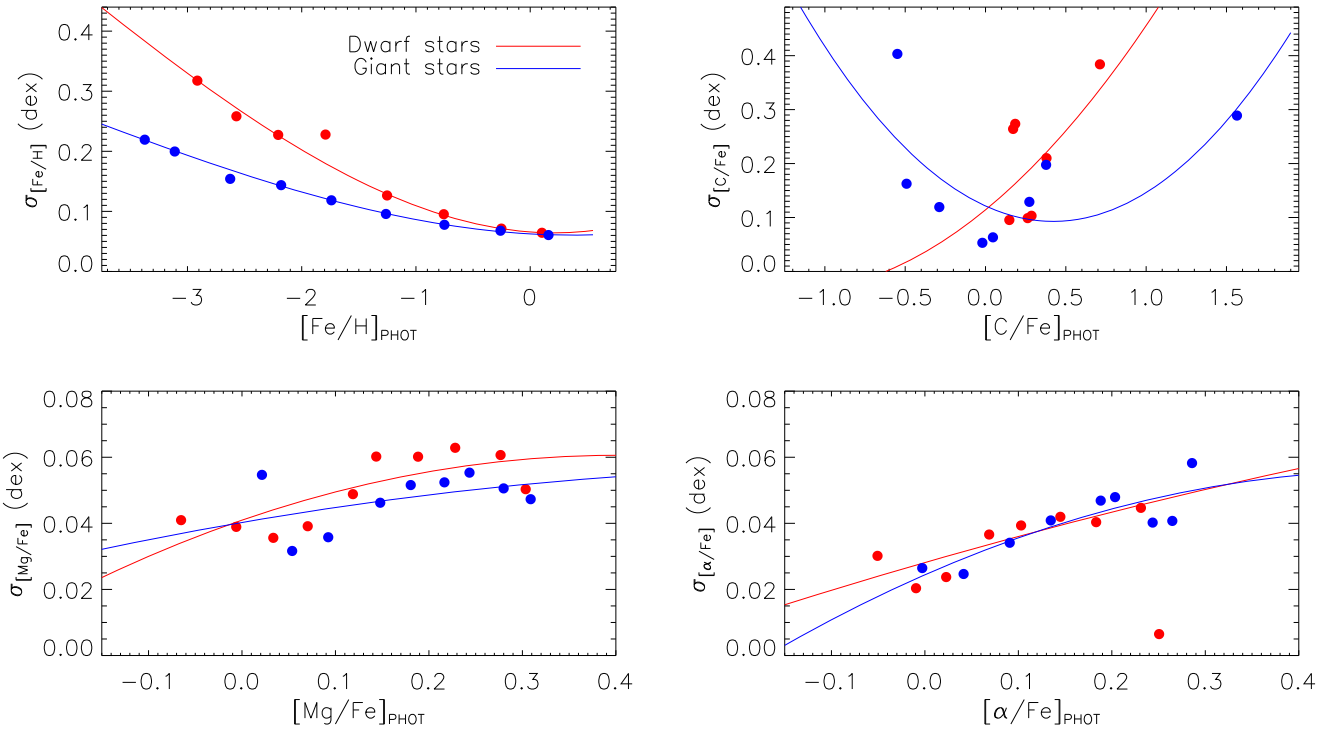

Figure 5. Uncertainties in the photometric estimates for [Fe/H] (top left), [C/Fe] (top right), [Mg/Fe] (bottom left), and [α/Fe] (bottom right), as functions of the photometric estimates, obtained using the training sets shown in Figures 3 and 4. The red and blue dots represent the results for dwarf and giant stars, respectively. The red and blue lines are second- and third-order polynomial fits to these data points, respectively.

stars are randomly selected from the millions of stars passing the above cuts. In total, 6183 dwarfs and 7052 giant stars are selected as the training sets for [Fe/H]; their metallicity distributions are shown in Figure 1. Clearly, the metallicity of our training sample can be extended to [Fe/H] ~ -4.0.

3.2. Carbon-to-Iron Abundance Ratios

Unlike for [Fe/H], there is no bibliographically compiled large catalog of [C/Fe] measurements from HRS observations covering the full range of [Fe/H] and [C/Fe] we consider here. We therefore adopt [C/Fe] measured from the SDSS/APOGEE survey as the reference scale. The comparison shown in Figure A5 indicates that the [C/Fe] measurements of the LAMOST/SEGUE VMP samples are consistent with those of SDSS/APOGEE, with negligible offsets and scatters of around 0.1 dex.[19] Again, the SDSS/APOGEE and LAMOST/SEGUE VMP samples are cross-matched with the J-PLUS parent sample to construct the training sets for [C/Fe]; the GALAH sample stars are used for test purposes. Here we note that evolution-dependent corrections (e.g., Placco et al. 2014) are not made for the adopted [C/Fe] estimates. The strategy for defining training stars is the same as we have used for [Fe/H]. In total, the [C/Fe] training set contains 5830 dwarfs and 6824 giant stars; their distributions in the [C/Fe] versus [Fe/H] space are shown in the upper panels of Figure 2. As found by many previous studies, the fraction of carbon-enhanced metal-poor (CEMP) stars ([C/Fe] $> +0.7$) increases rapidly with decreasing [Fe/H].

[19] The scatter is slightly larger, around 0.3 dex, for the LAMOST VMP samples.

3.3. Magnesium-to-Iron and α-to-Iron Abundance Ratios

Similar to [C/Fe], [Mg/Fe] and [α/Fe] from the SDSS/APOGEE survey are adopted for the reference scales. The results from GALAH are quite consistent with those from SDSS/APOGEE, as shown in Figure A5. The uncertainties of [Mg/Fe] and [α/Fe] in the LAMOST/SEGUE VMP samples are quite large; thus they are not adopted in the training sets. The lack of VMP sample stars in our training sets may introduce issues for estimating [Mg/Fe] and [α/Fe] for VMP stars, which are discussed in Section 4.4. Finally, 4034 dwarfs and 4984 giant stars are chosen for the training sets of [Mg/Fe] (middle panels in Figure 2); 4041 dwarfs and 4990 giant stars are selected for the training sets of [α/Fe] (bottom panels in Figure 2). The GALAH sample stars are again adopted for checking the precision of estimation of [Mg/Fe] and [α/Fe].

4. Estimates of [Fe/H], [C/Fe], [Mg/Fe], and [α/Fe] from the J-PLUS and Gaia Colors

4.1. Kernel Principal Component Analysis

Principal component analysis (PCA) is widely used in astronomy for transforming observational features (e.g., spectra, multiple colors) to a set of uncorrelated orthogonal principal components. Kernel principal component analysis (KPCA; Schölkopf et al. 1998) is an extension of PCA, which adds a kernel technique for nonlinear feature extraction. This approach has been applied to estimate stellar parameters, including atmospheric parameters, mass, and age, from stellar spectra (e.g., Huang et al. 2015, 2020; Xiang et al. 2017; Wu et al. 2019). Here we adopt the KPCA technique[20] to derive metallicity and elemental-abundance ratios (i.e., [C/Fe],

[20] Here we set the kernel to be a Gaussian radial basis function.

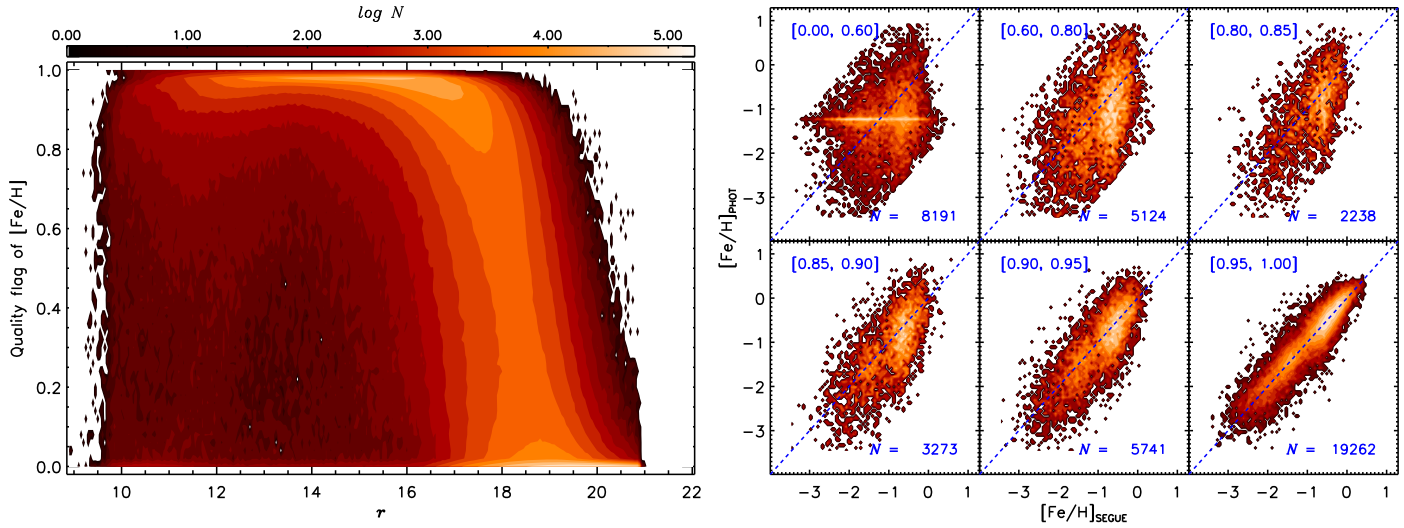

Figure 6. Left panel: density distribution of the [Fe/H] quality flag $\texttt{flg}_{\rm [Fe/H]}$ as a function of r-band magnitude. A color bar representing the numbers of stars is provided at the top of the panel. Right panel: comparisons of the photometric metallicity and the SDSS/SEGUE spectroscopic metallicity for different ranges of the [Fe/H] quality flag (as marked in the top left corner of each subpanel). The SDSS/SEGUE spectroscopic metallicity is corrected for the systematic offsets described in Appendix A. The blue dashed lines are the one-to-one lines. The total number of stars used in the comparison is marked in the bottom right corner of each subpanel.

[Mg/Fe], and [α/Fe]) from the multiple colors formed with the combination of J-PLUS DR3 and Gaia EDR3 (Gaia Collaboration et al. 2021) magnitudes. The number of principal components and the radius of the Gaussian radial basis are chosen by a series of tests to achieve a tradeoff between reducing the training residuals and avoiding overfitting.

4.2. Training Results

To derive photometric estimates of metallicity and elemental-abundance ratios, 13 stellar colors: $G_{\rm BP}-G_{\rm RP}$, $G_{\rm BP}-u$, $G_{\rm BP}-g$, $G_{\rm RP}-r$, $G_{\rm RP}-i$, $G_{\rm RP}-z$, $G_{\rm BP}-$J0378, $G_{\rm BP}-$J0395, $G_{\rm BP}-$J0410, $G_{\rm BP}-$J0430, $G_{\rm BP}-$J0515, $G_{\rm RP}-$J0660, and $G_{\rm RP}-$J0861 are used as observational inputs. All the colors are dereddened using the SFD extinction map, as well as the extinction coefficients described in Section 2.2. With the KPCA technique, we construct the relations between the stellar labels from the aforementioned training sets and these 13 colors.

The training results for [Fe/H] and [C/Fe] are shown in Figure 3; those for [Mg/Fe] and [α/Fe] are shown in Figure 4.

Generally, the trained photometric estimate of metallicity is consistent with the spectroscopic estimate, even at the metal-poor end, down to [Fe/H] ~ -4.0. No significant offsets are detected down to [Fe/H] $= -2.5$, while small deviations (-0.10 to -0.25 dex) are found at the more metal-poor end. The dispersion is tiny (<0.10 dex) for the metal-rich region ([Fe/H] > -1.0), and 0.10–0.30 dex for the metal-poor region ([Fe/H] < -1.0). We note that, overall, the [Fe/H] precision for giant stars is better than that for dwarf stars, especially at the metal-poor end, as is expected due to the weaker absorption lines for the warmer dwarfs.

The photometric [C/Fe] estimates for dwarf stars have moderate offsets in both the carbon-rich region ([C/Fe] $> +1.0$; the offset is around $+0.5$ dex in the sense spectroscopic minus photometric) and the carbon-poor region ([C/Fe] < -0.5; the offset is around -0.5 dex). The precision is also a function of [C/Fe]: about 0.05–0.10 dex in the middle region ($-0.5 <$ [C/Fe] $< +0.5$), and up to 0.2–0.4 dex at the carbon-rich/poor ends. For giant stars, the photometric [C/Fe] estimate is quite good compared to the spectroscopic one; no significant offset is detected. The precision is about 0.05–0.10 dex for the middle region ($-0.5 <$ [C/Fe] $< +0.5$) and 0.15–0.25 dex for the carbon-rich and carbon-poor ends.

For [Mg/Fe] and [α/Fe], the photometric estimates agree with the spectroscopic ones, with precision better than 0.05 dex for both dwarf and giant stars, although slight offsets are found in the high [Mg/Fe] and [α/Fe] ranges. The overall precision of [α/Fe] is slightly better than that of [Mg/Fe]. The scatter of the comparisons between the photometric and spectroscopic estimates for these parameters, as a function of the photometric estimates, is shown in Figure 5.

Finally, at the suggestion of the referee, we clarify the error levels associated with our determinations of [Fe/H], [Mg/Fe], and [α/Fe]. Our estimates are based on the labels from spectroscopy, in particular from the HRS; thus the errors are "inherited" from the labels used for the calibration stars. The best precision we can achieve is thus close to that of the HRS. For the [Fe/H] HRS measurements, the error comes from two sources: (1) a statistical error from the scatter of measurements for different iron lines, and (2) a systematic error from the uncertainties in the atmospheric parameters (which can differ somewhat between different subsamples in the HRS). In most cases, the latter one dominates the total error of the [Fe/H] determinations (e.g., a typical 100 K $T_{\rm eff}$ error will result in about a 0.1 dex error in [Fe/H] for stars of solar abundance). For [Mg/Fe] or [α/Fe], the origin of the error is the same as that due to [Fe/H]. The statistical error is similar to that for [Fe/H]; the systematic error is largely reduced since, using Fe as the reference element, Mg shares similar systematics. This accounts for why the uncertainty of [Fe/H] is larger than that of [Mg/Fe] and [α/Fe].

4.3. Application to the J-PLUS Parent Sample

The above trained relationships are applied to the J-PLUS parent sample of $\sim$16.5 million stars defined in Section 2.2. To evaluate the quality of the estimated abundances, we define the quality parameter $\texttt{flg}_x$ (here x represents [Fe/H], [C/Fe], [Mg/Fe], or [α/Fe]), which is given by the maximal kernel value between the target stellar colors and those in the training set. The value of $\texttt{flg}_x$ can vary from 0 to 1, with unity

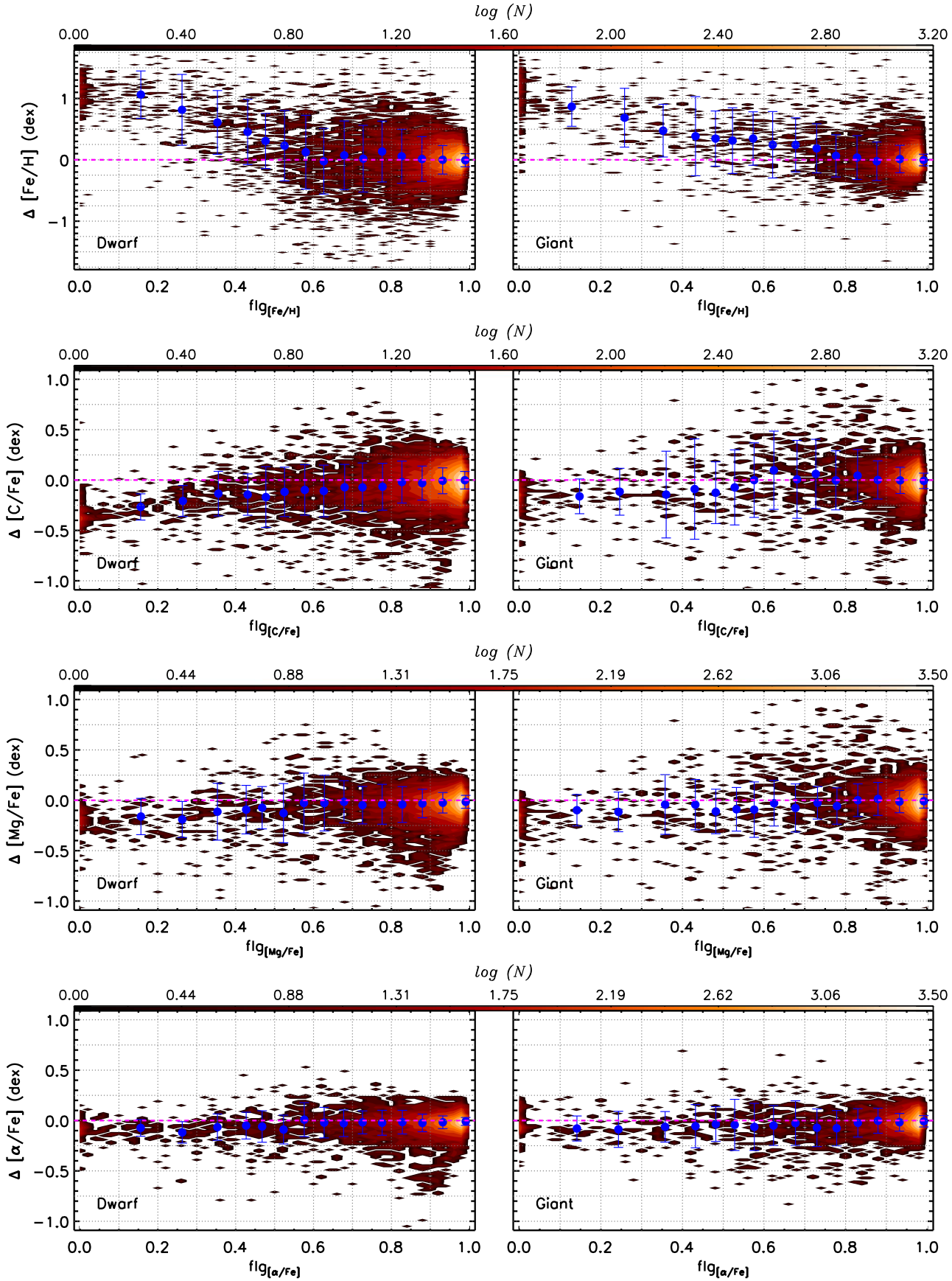

Figure 7. Density distributions of the metallicity and elemental-abundance differences (APOGEE estimates minus photometric estimates) as a function of the quality flag for [Fe/H] (first row), [C/Fe] (second row), [Mg/Fe] (third row), and [α/Fe] (bottom row). The left column is for dwarf stars and the right column is for giant stars. The blue dots and error bars in each panel represent the median and dispersion of the parameter differences in the individual bins of the parameter quality flag. Magenta dashed lines indicate zero residuals in each panel. A color bar representing the numbers of stars is provided at the top of each row of panels.

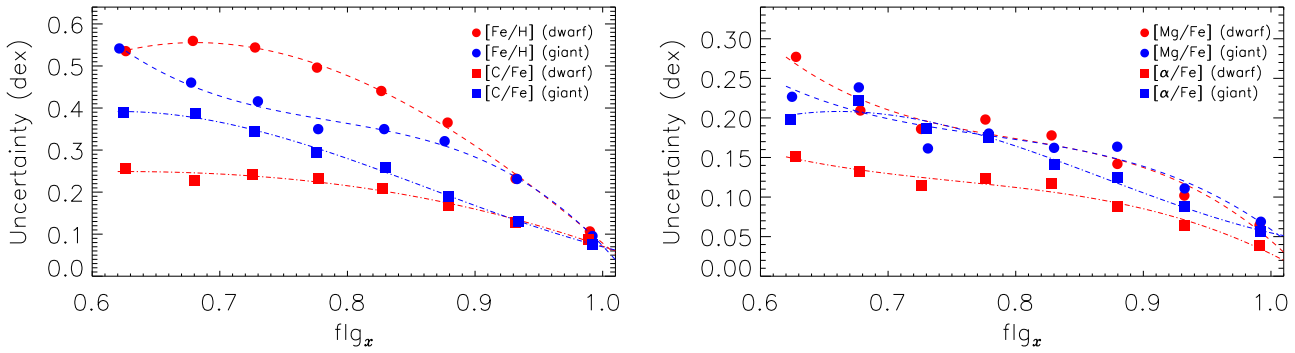

Figure 8. Uncertainties of photometric estimates for [Fe/H] and [C/Fe] (left panel), and [Mg/Fe] and [α/Fe] (right panel), derived from comparison with the APOGEE–J-PLUS stars in common, as a function of the photometric quality flags, $\texttt{flg}_x$. Red and blue symbols represent the results for dwarf and giant stars, respectively. The dashed lines represent third-order polynomial fits to these data points.

representing exact agreement between the target stellar colors and those in the training set. As an example, Figure 6 shows the distribution of $\texttt{flg}_{\rm [Fe/H]}$ as a function of r-band magnitude. As expected, $\texttt{flg}_{\rm [Fe/H]}$ is close to 1 for stars brighter than $r = 18$, and quickly drops to 0 at the faint end due to the larger photometric errors. We note that a small fraction of stars may have low values of $\texttt{flg}_{\rm [Fe/H]}$ in the bright range, likely due to stellar variability, binarity, emission-line objects, etc.

We also compare the J-PLUS photometric-metallicity estimates to those from SDSS/SEGUE medium-resolution spectroscopy in different bins of $\texttt{flg}_{\rm [Fe/H]}$ (see right panel of Figure 6). Generally, the dispersion of the metallicity difference between the photometric and spectroscopic estimates increases with decreasing $\texttt{flg}_{\rm [Fe/H]}$. For $\texttt{flg}_{\rm [Fe/H]} < 0.60$, the dispersion is larger than 0.8 dex, and obvious artificial features are seen; thus, the photometric estimates of metallicity are not recommended for any stars with $\texttt{flg}_{\rm [Fe/H]} < 0.60$.

After removing stars used in the training sets, the remaining APOGEE–J-PLUS stars in common are used to consider the abundance differences (spectroscopic minus photometric), as a function of $\texttt{flg}_x$, in Figure 7. Clearly, the scatter increases with decreasing $\texttt{flg}_x$ for all estimated abundances (see Figure 8), i.e., [Fe/H], [C/Fe], [Mg/Fe], and [α/Fe]. The trends fitted by third-order polynomials can be taken as the random error of the abundance estimate σ_x. By considering the fitting uncertainty (hereafter, the method error σ_m) as a function of the abundances themselves in Figure 5, the final uncertainty of the abundance measurement for a specific star is given by $\sqrt{\sigma_x^2 + \sigma_m^2}$. In total, over five million stars have determinations of stellar abundances with at least one parameter quality flag ($\texttt{flg}_x$) greater than 0.6 (hereafter referred to as the J-PLUS parameter sample); the total number is about 4.8 million if all quality flags are required to satisfy $\texttt{flg}_x \geqslant 0.6$.

4.4. Validation

4.4.1. Comparison with GALAH DR3

As mentioned in Section 3, stars from the GALAH survey are not used in the training sets, and thus can be adopted to examine our photometric estimates. The GALAH DR3 is cross-matched with the J-PLUS parameter sample, by requiring GALAH $\texttt{SNR\_C2\_IRAF} \geqslant 30\,\mathrm{pixel}^{-1}$ and J-PLUS $\texttt{flg}_x \geqslant 0.9$. The comparison results are shown in Figure 9. For [Fe/H], our photometric results are in excellent agreement with the HRS estimates from GALAH, with negligible offsets and scatter of around 0.10 dex for both dwarf and giant stars. Generally, the photometric [Mg/Fe] estimates agree with those from GALAH, with a moderate scatter of 0.08 dex. The comparisons show that the photometric estimate of [α/Fe] is quite precise, with scatter of only 0.05 dex for dwarf stars and 0.06 dex for giant stars. This is also in line with our training results, as shown in Figure 4.

4.4.2. Comparison with the LAMOST Medium-resolution Survey

Most recently, Li et al. (2023) derived stellar parameters from over 4 million LAMOST medium-resolution ($R \sim 7500$) spectra using the RRNet technique and the APOGEE DR17 stellar parameters as training labels. This sample is cross-matched with the J-PLUS parameter sample, by requiring $\texttt{SNR\_BLUE} \geqslant 20\,\mathrm{pixel}^{-1}$, J-PLUS $\texttt{flg}_{\rm [Fe/H]} \geqslant 0.9$, and Gaia $\texttt{RUWE} < 1.4$. In total, 53,676 stars in common are found. Generally, our photometric estimates agree very well with those of Li et al. (2023), with negligible offsets and a small scatter around 0.09 dex for both dwarf and giant stars (see Figure 10). However, we note that their metallicity estimates are truncated at [Fe/H] $= -1.0$ for dwarf stars and [Fe/H] $= -1.5$ for giant stars (see Figure 10).

4.4.3. Comparison with Metal-poor Samples from the Literature

The identification of large numbers of metal-poor stars is one of the main goals of this project. We therefore want to compare our photometric abundance estimates to those derived from spectroscopy in the literature.

First, our photometric abundances are compared to those for low-metallicity candidates from the Best & Brightest (B&B) Survey with medium-resolution ($R \sim 2000$) follow-up spectroscopic observations (Schlaufman & Casey 2014). More recently, Placco et al. (2019) and Limberg et al. (2021) present metallicity estimates, along with other elemental-abundance ratios ([C/Fe] and [Mg/Fe]), for nearly 1900 stars using the medium-resolution spectra from follow-up of stars in the B&B survey.[21] In total, 37 metal-poor ([Fe/H] $\leqslant -1.5$) giant stars in common (with $\texttt{flg}_{\rm [Fe/H]} \geqslant 0.9$, $\texttt{flg}_{\rm [C/Fe]} \geqslant 0.9$, or $\texttt{flg}_{\rm [Mg/Fe]} \geqslant 0.9$) are found, with the lowest metallicity approaching [Fe/H] ~ -3.0. Moderate offsets of -0.11 dex (B&B minus photometric estimates) are found in the metallicity differences, as shown in Figure 11. The scatter is only 0.15 dex, consistent with the expectation from our internal check shown in Figure 5

[21] Note that the spectroscopic abundance ratios for [C/Fe] and [Mg/Fe] or [α/Fe] reported by Placco et al. (2019) and Limberg et al. (2021) have been superseded by the values listed in Shank et al. (2022), who corrected an error that existed in their calculation in the previous works.

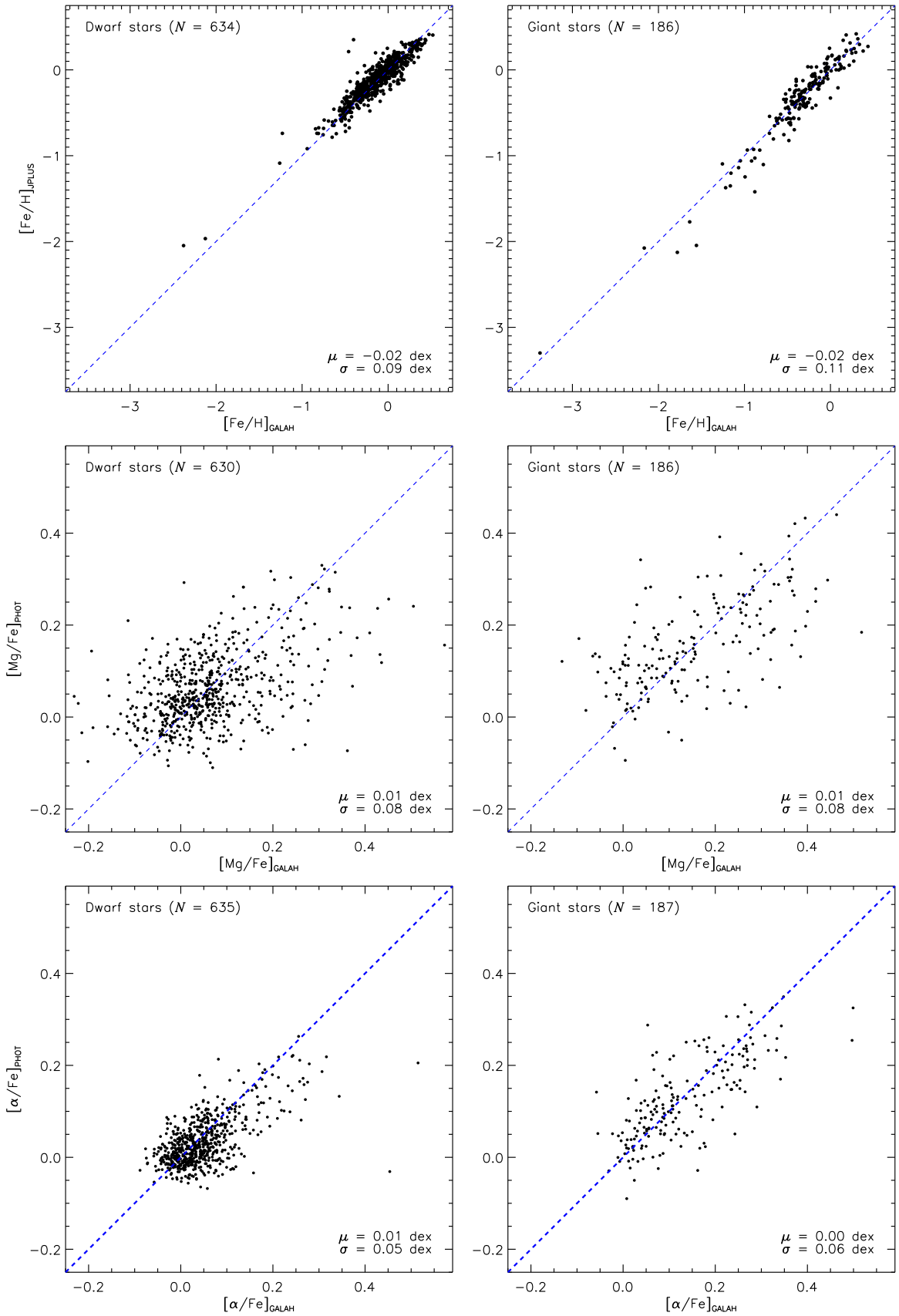

Figure 9. Comparisons of the photometric estimates of [Fe/H] (top panels), [Mg/Fe] (middle panels), and [α/Fe] (bottom panels) with spectroscopic estimates from GALAH DR3. The left column applies to dwarf stars and the right column to giant stars. The blue dashed lines are the one-to-one lines. The overall median offset and standard deviation are marked in the bottom right corner of each panel.

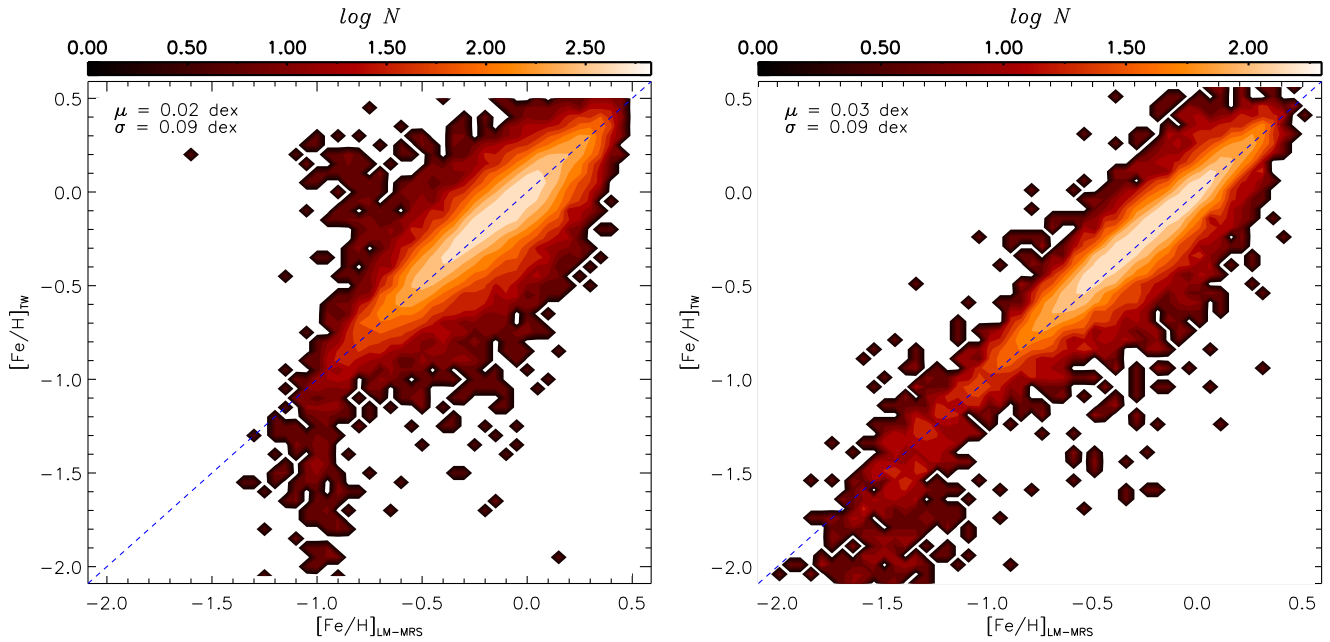

Figure 10. Comparisons of the photometric estimates with those from Li et al. (2023) for dwarf stars (left panel) and giant stars (right). The blue dashed lines are the one-to-one lines. The overall median offset and standard deviation are marked in the top left corner of each panel. Color bars representing the numbers of stars are provided at the top of each panel.

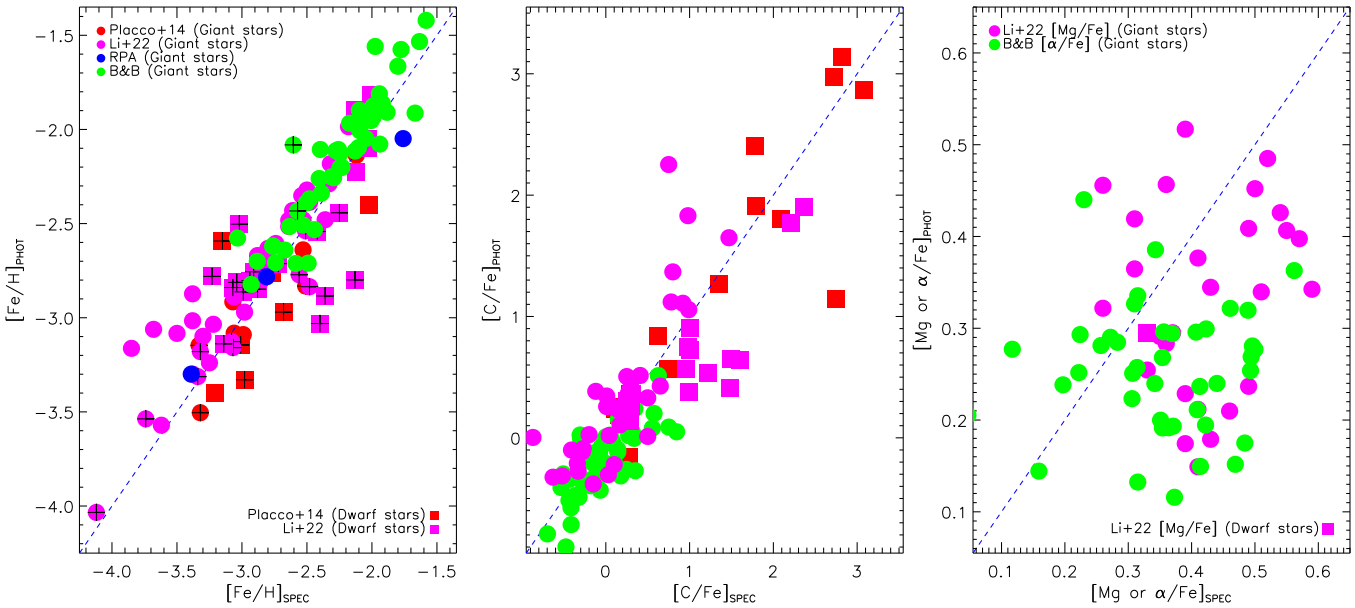

Figure 11. Comparisons of the photometric estimates of [Fe/H] (left panel), [C/Fe] (middle panel), and [Mg/Fe] or [α/Fe] (right panel) with those from the Best & Brightest Survey (green dots; Schlaufman & Casey 2014) and the HRS samples. The CEMP stars are from Placco et al. (2014, red dots), the *R*-Process Alliance sample (blue dots; Hansen et al. 2018; Sakari et al. 2018; Ezzeddine et al. 2020; Holmbeck et al. 2020), and the Subaru follow-up observations of LAMOST VMP candidates (magenta dots; Aoki et al. 2022; Li et al. 2022). In the left panel, the plus symbols mark the CEMP stars with [C/Fe] $> +0.7$. The blue dashed lines are the one-to-one lines.

(see Section 4.2). Generally, the photometric estimate of [C/Fe][22] agrees with that of the B&B follow-up, with a moderate offset of +0.13 dex and scatter of 0.19 dex. The scatter of the [α/Fe] difference is large; this is as expected, due to the lack of metal-poor stars with precise estimates of [Mg/Fe] in our training sets (see Section 3.3).

Second, photometric abundances are compared to the HRS sample stars, only a few of which are included in our training sets. The HRS sample stars are collected from the CEMP sample for over 600 stars (Placco et al. 2014), the *R*-Process Alliance project (Hansen et al. 2018; Sakari et al. 2018; Ezzeddine et al. 2020; Holmbeck et al. 2020) for over 600 VMP stars, and the 400 LAMOST-selected VMP candidates with chemical abundances determined from Subaru high-resolution spectroscopic follow-up (Aoki et al. 2022; Li et al. 2022). In total, there are 79 stars in common (28 dwarf and 51

[22] The [C/Fe] estimates refer to results without evolution-dependent corrections, since no such corrections were made for the training sets (see Section 3.2).

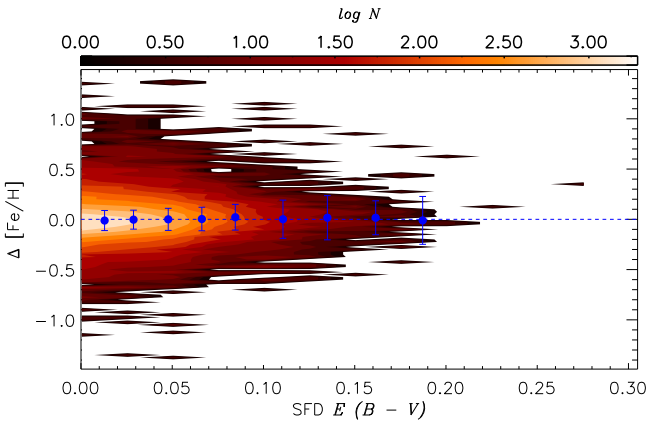

Figure 12. Density distributions of the metallicity difference for APOGEE–J-PLUS, as a function of SFD $E(B-V)$. The blue dashed line indicates zero residuals. The blue dots and error bars represent the median and dispersion of the metallicity difference in the individual bins of SFD $E(B-V)$ reddening estimate. No trend of the metallicity difference with SFD $E(B-V)$ is detected. The color bar at the top of represents the numbers of stars.

giant stars) with $\texttt{flg}_{\rm [Fe/H]}$ greater than 0.9, covering a metallicity range of $[{\rm Fe/H}]=[-4.0,\ -2.0]$. For [Fe/H], the median difference is minor for both dwarf and giant stars; the scatter is 0.32 dex for dwarf stars and about 0.17 dex for giant stars, which is consistent with the performance of the training exercise (see Figure 5).

Of central importance, unlike in the case for SMSS and SAGES (which only employ two narrow/medium-band filters, the u and v bands), our photometric metallicities for CEMP stars (those with pluses in Figure 11) are no longer overestimated, since the J0395 filter responds to metallicity, while the J0430 filter independently measures the molecular carbon centered on the CH G band. Among the 73 stars in common (25 dwarf and 48 giant stars) with $\texttt{flg}_{\rm [C/Fe]}\geqslant 0.9$, almost all the CEMP stars with $[{\rm C/Fe}]>+0.7$ in the HRS sample are recovered by our photometric measurements. The median offset (HRS minus photometric) of [C/Fe] is minor for giant stars and 0.44 dex for dwarf stars, similar to that found for our training sets (bottom panels of Figure 3). The overall scatter of the [C/Fe] difference is 0.52 dex for dwarfs and 0.27 dex for giant stars. Again, as expected, the scatter of the difference between the photometric and HRS estimates of [Mg/Fe] or [α/Fe] is quite large.

4.4.4. Examination of Metallicity Systematics in Relation to Reddening

As mentioned in Section 2.2, we adopted the SFD map to correct the extinction since most of sample stars (92.7%) are located in regions of low extinction with $E(B-V)<0.1$. However, the SFD map is a two-dimensional map, and the reddening of nearby stars may be overestimated. To examine this potential systematic, the J-PLUS sample is cross-matched with the DR17 of APOGEE.[23] By requiring APOGEE spectral $\texttt{SNR}\geqslant 50$, J-PLUS $\texttt{flg}_{\rm [Fe/H]}\geqslant 0.9$, and Gaia $\texttt{RUWE}<1.4$, a total of 32,088 stars in common are found. Figure 12 shows the metallicity difference (APOGEE minus J-PLUS), as a function of SFD $E(B-V)$. The median offsets are almost zero for different bins of $E(B-V)$, ranging from 0 to 0.20. This result confirms that the SFD map is sufficiently accurate for photometric estimates of stellar parameters, as expected given the low extinction values for most of the sample stars.

[23] We note that only a few thousand stars with extremely low extinction values of $E(B-V)<0.04$ were used as the training sample. Therefore, it is appropriate to reexamine the metallicity difference with $E(B-V)$ using APOGEE stars.

4.5. Comparisons with Previous Estimates from J-PLUS DR1 and DR2

Prior to this work, several attempts have provided estimates of stellar parameters, as well as elemental abundances, from J-PLUS DR1 (Whitten et al. 2019; Yang et al. 2022) and DR2 (Galarza et al. 2022). Based on J-PLUS DR1, stellar parameters and [C/Fe], [N/Fe], [Mg/Fe], [Ca/Fe], and [α/Fe] are derived for two million stars (Yang et al. 2022, hereafter Yang+22). As shown in the left panel of Figure 13, our metallicity is consistent with that of Yang+22 with a negligible offset of −0.03 dex (this work minus Yang+22) and a scatter of 0.14 dex. At the metal-poor end, the metallicity of Yang+22 is overestimated and truncated at $[{\rm Fe/H}]\sim -2.5$ due to their training labels from LAMOST DR5 (see Figure A2). The estimates of [C/Fe], [Mg/Fe], and [α/Fe] are also compared to those from Yang+22 in Figure 14. Generally, they agree with each other within the typical errors. By using the Sellar Parameters Estimation based on Ensemble Methods (SPEEM) pipeline, Galarza et al. (2022) have derived stellar atmospheric parameters ($T_{\rm eff}$, $\log g$, and [Fe/H]) for a "gold sample" of 746,531 stars from J-PLUS DR2. The comparison of our photometric estimates of [Fe/H] to those from Galarza et al. (2022) is shown in the right panel of Figure 13. The median difference is 0.05 dex (this work minus SPEEM) and the scatter is only 0.10 dex. Similarly, the metallicity estimated by SPEEM is overestimated at the metal-poor end ($[{\rm Fe/H}]<-2.0$), which has been already mentioned in Galarza et al. (2022).

4.6. Comparisons with Other (Spectro)photometric Estimates

In this subsection, the J-PLUS metallicity estimates are compared to other photometric results from surveys that employ one/two blue narrowband filters, those from the SAGES DR1 (Paper II), the SMSS DR2 (Paper I), and the Pristine Survey DR1 (Martin et al. 2023).

Due to contamination of the blue narrow/medium-band filters by molecular carbon bands such as CN, the photometric estimates of [Fe/H] are often overestimated for VMP stars—the most interesting targets for understanding the early chemical evolution of the Universe. This is due to the large fraction of VMP stars that are carbon-enhanced, causing the colors ($u/v-G_{\rm BP}$) to appear redder than for a VMP star with normal carbon abundance (Starkenburg et al. 2017; Papers I and II). As discussed earlier, owing to the use of the seven narrow/medium-band filters employed by J-PLUS, the above degeneracy can be broken; the metallicity and [C/Fe] can both be photometrically measured.

Generally, the SAGES, SMSS, and Pristine [Fe/H] estimates are quite consistent with those from J-PLUS (see Figure 15), with scatters of ∼0.20 dex for dwarf stars and ∼0.15 dex for giant stars. There is an offset of 0.10–0.15 dex between J-PLUS and Pristine (former minus latter). As compared to the J-PLUS estimates, the SAGES, SMSS, and Pristine [Fe/H] estimates exhibit strong biases for carbon-enhanced stars; their [Fe/H] estimates are overestimated by 1–2 dex at $[{\rm C/Fe}]\geqslant +1.0$ for both dwarf and giant stars (see Figure 15).

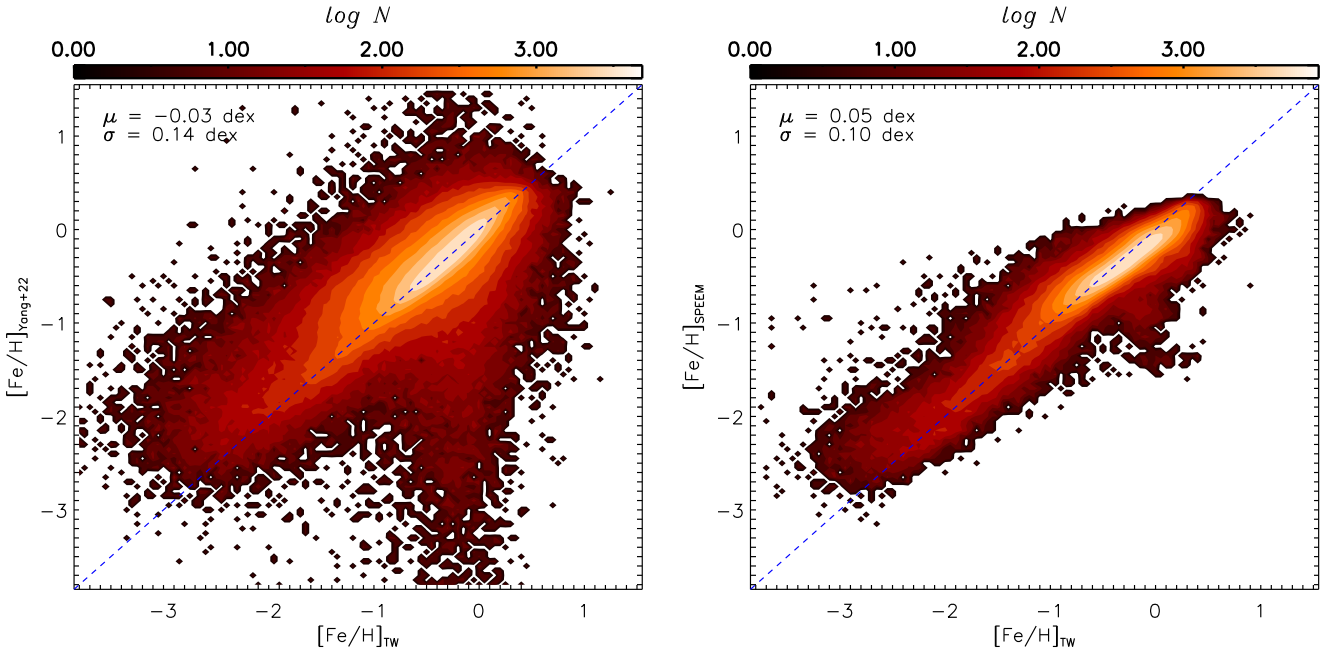

Figure 13. Comparisons of the photometric estimates of [Fe/H] with those from Yang et al. (2022, left panel) and those from Galarza et al. (2022, right panel) using around 0.5 million stars in common. The blue dashed lines are the one-to-one lines. The overall median offset and standard deviation are marked in the top left corner of each panel. Color bars representing the numbers of stars are provided at the top of each panel.

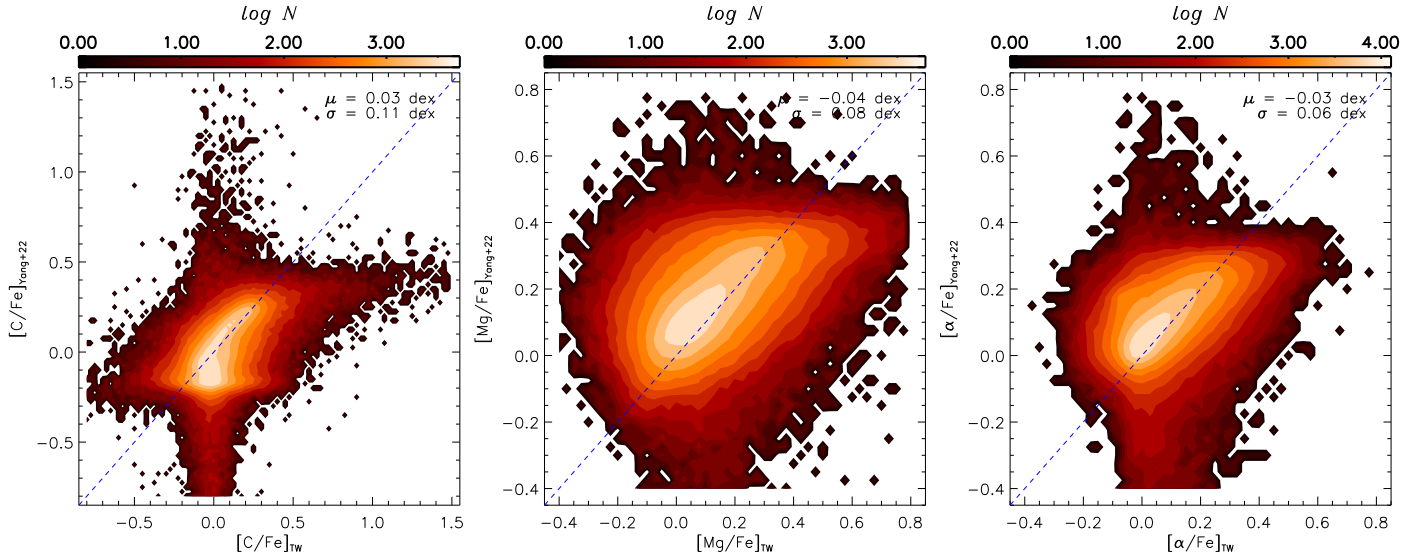

Figure 14. Comparisons of the photometric estimates of [C/Fe] (left panel), [Mg/Fe] (middle panel), and [α/Fe] (right panel) to those from Yang et al. (2022), using the approximately 0.5 million stars in common. The blue dashed lines are the one-to-one lines. The overall median offset and standard deviation are marked in the top right corner of each panel. Color bars representing the numbers of stars are provided at the top of each panel.

Unexpectedly, the XP metallicity estimates (Andrae et al. 2023) exhibit similar trends along with [C/Fe], when compared to the J-PLUS metallicity estimates. In principle, the XP spectra contain sufficient information to determine [Fe/H] and [C/Fe] simultaneously (see Lucey et al. 2023). One possible explanation is that there are few carbon-enhanced stars in their training sets.

5. Effective Temperatures, Distances, Ages, and Surface Gravities

Through use of the metallicity-dependent $T_{\rm eff}$–color relations constructed in Paper I of this series, the effective temperatures for J-PLUS dwarf and giant stars are derived from $(G_{\rm BP} - G_{\rm RP})_0$ and the photometric [Fe/H] estimated above. As shown in Paper II, the typical uncertainty of the derived effective temperature is within 100 K when compared to the spectroscopic uncertainty. For instance, as examined with over 400,000 common stars, the effective temperature estimated in this work is quite consistent with that from LAMOST, with a tiny offset of around 14 K (LAMOST minus this work) and a scatter of only 72 K (see Figure 16).

The strategy of distance determinations is again similar to that described in Papers I and II. For stars with reliable parallax measurements from Gaia EDR3 (precision better than 30%, parallax greater than 0.15 mas, and renormalized unit weight error (RUWE) smaller than 1.4), the distances are directly

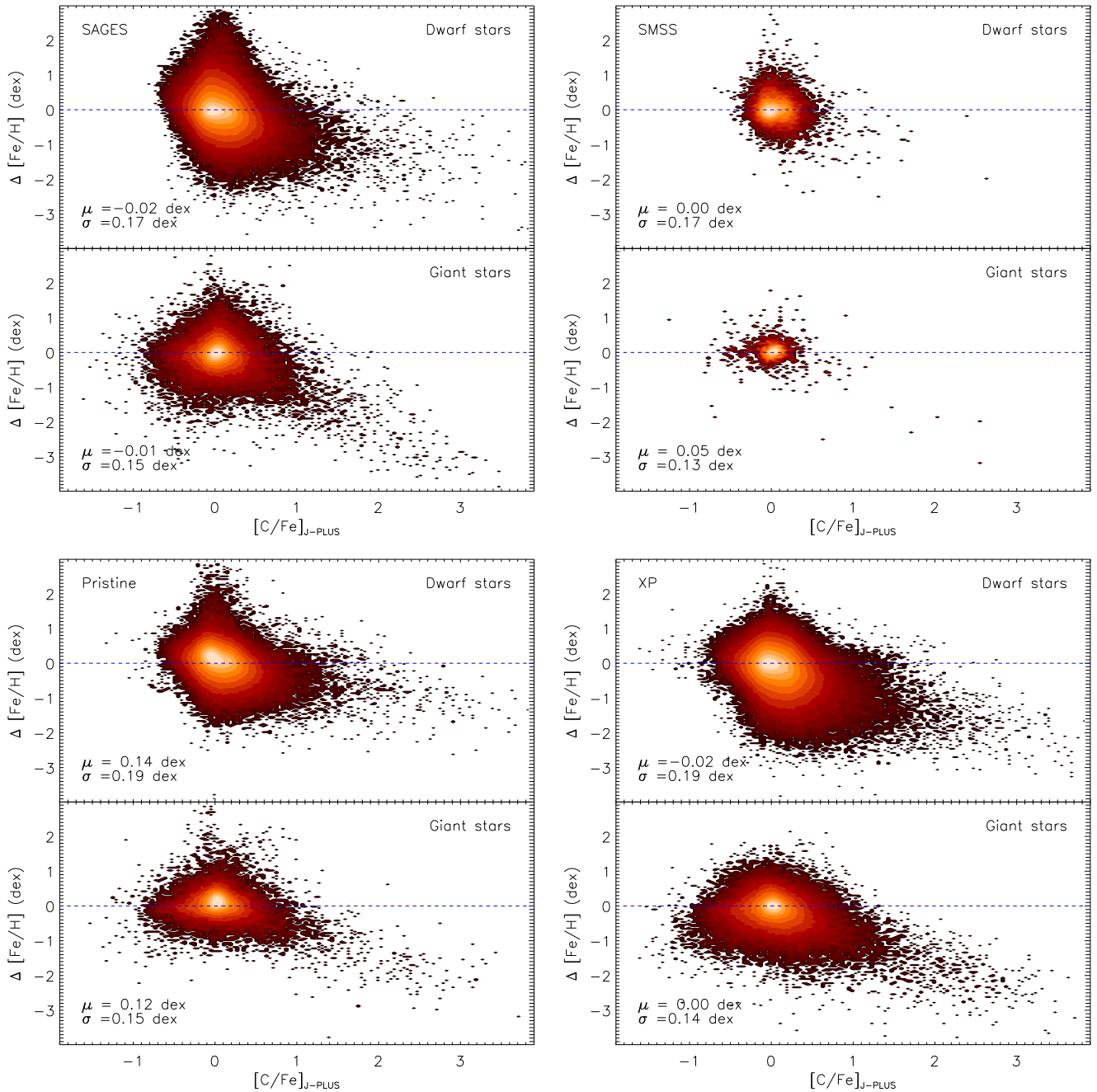

Figure 15. Density distributions of the metallicity differences for J-PLUS–SAGES (top left), J-PLUS–SMSS (top right), J-PLUS–Pristine (bottom left), and J-PLUS–Gaia XP (bottom right), as a function of J-PLUS photometric [C/Fe]. Blue dashed lines indicate the zero residuals in each panel. The overall median offset and standard deviation are marked in the bottom left corner of each panel.

adopted from Bailer-Jones et al. (2021). The further classifications (turnoff, main sequence, and binary; see subtype in Table 2), based on positions of the stars on the Hertzsprung–Russell diagram, are obtained by comparison with the PARSEC isochrones (Bressan et al. 2012; Marigo et al. 2017).

Using a Bayesian method similar to that in Paper I, the stellar ages for stars are determined with the constraints from $(G_{\rm BP} - G_{\rm RP})_0$, G-band absolute magnitude, and photometric metallicity. In this work, the surface gravity is also estimated using the isochrone-fitting technique described above. In this manner, nearly 3.8 million stars have their distances, ages, and surface gravities, as well as luminosity classifications, assigned.

As mentioned in Paper I, the isochrone-fitting method mainly works for turnoff stars with a typical uncertainty of 20%. For distant dwarf and giant stars, the empirical metallicity-dependent color–absolute magnitude relations/fiducials from Paper I are adopted. Interested readers are referred to Paper I for additional details. By combining with Gaia and Pan-STARRS photometry, and the SFD reddening map, distances for around 0.5 million distant stars are estimated. This is important for stars in our giant sample, since 40% of their distances are derived in this way. As examined from nearly 700 stars in common with the SDSS/SEGUE sample of K giants (Xue et al. 2014), the precision of our distances from the color–absolute magnitude fiducials is better than 16%, without

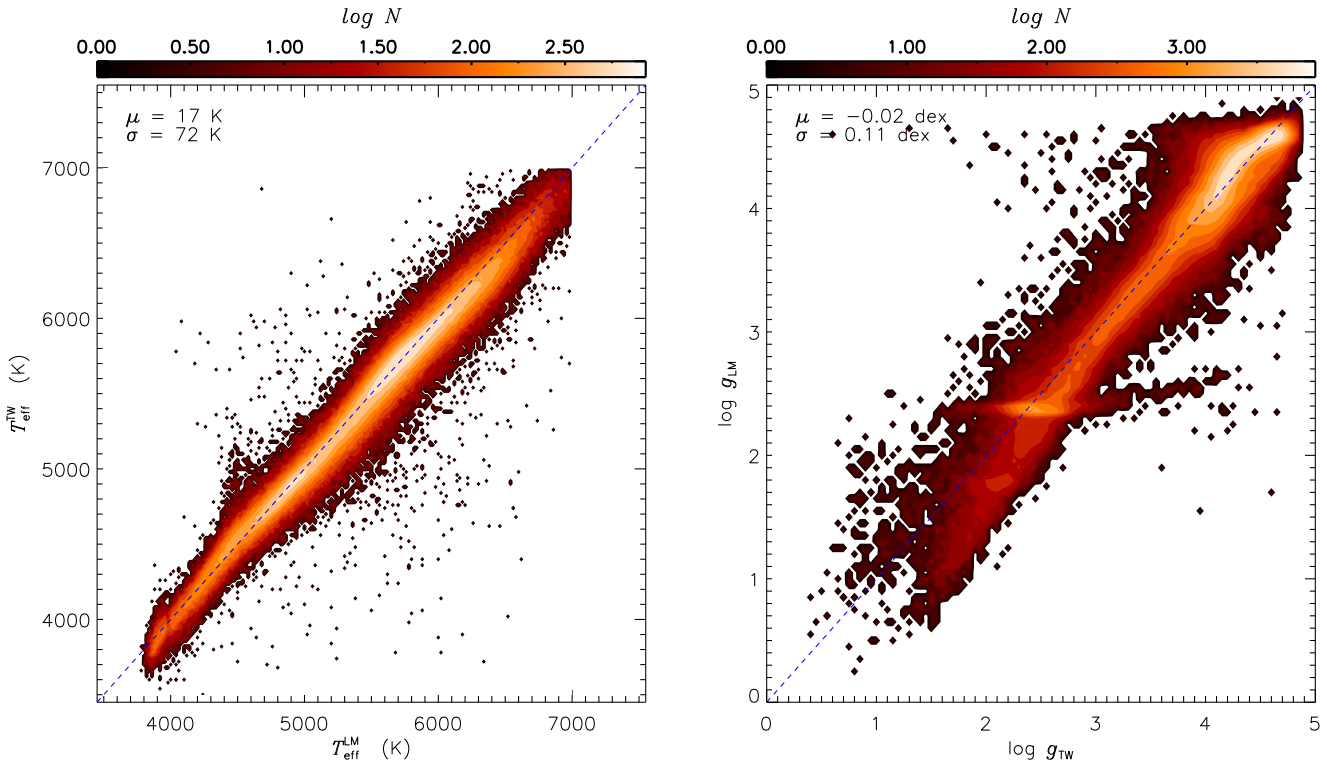

Figure 16. Comparisons of our estimates of $T_{\rm eff}$ (left panel) and log g (right panel) to those from DR9 of the LAMOST low-resolution survey. The blue dashed lines are the one-to-one lines. The overall median offset and standard deviation are marked in the top left corner of each panel. Color bars representing the numbers of stars are provided at the top of each panel.

significant offsets. Again using over 400,000 stars in common, the surface gravity estimated in this work is also consistent with that of the LAMOST spectroscopic survey, with a tiny offset of −0.02 dex (LAMOST minus this work) and a scatter of only 0.11 dex (see Figure 16).

6. The J-PLUS Parameter Sample

Using data from J-PLUS DR3 and Gaia EDR3, the photometric metallicity, carbon-to-iron abundance ratio, magnesium-to-iron abundance ratio, and alpha-to-iron abundance ratio are estimated for about 4.5 million dwarf and 0.5 million giant stars with quality flags $\texttt{flg}_x > 0.6$. Their spatial coverage and magnitude distributions are shown in Figure 17.

The metallicity distribution functions (MDFs) for dwarf and giant stars are shown in Figure 18. In total, over 160,000 VMP stars are found. As an example of the utility of these VMP stars, we investigate the MDFs of the metal-poor halo stars for the sample of J-PLUS giant stars. The slope is found to be $\frac{\Delta N}{\Delta\,[{\rm Fe/H}]} = 1.30 \pm 0.05$ and $\frac{\Delta N}{\Delta\,[{\rm Fe/H}]} = 1.12 \pm 0.05$, respectively, for the inner stellar halo ($r < 25$ kpc and $|Z| > 5$ kpc) and the outer stellar halo ($r > 25$ kpc and $|Z| > 5$ kpc) with [Fe/H] between −2.75 and −4.0. The result found for the inner halo is commensurate with other recent determinations (e.g., Youakim et al. 2020; Shank et al. 2021; Yong et al. 2021). This first application shows that the slope of the MDF may evolve with r, which is worth exploring further with the (presumably minimal) selection effects properly considered.

We also show the [C/Fe] versus [Fe/H] distributions of our sample in Figure 19. As found by previous studies, carbon-enhanced stars ([C/Fe] > +0.7) are mostly found in the metal-poor regime ([Fe/H] ⩽ −1.0); they are therefore referred to as CEMP stars. The fraction of CEMP stars is a strong increasing function of declining [Fe/H], with a value of a few percent at [Fe/H] ∼ −1.0 to as high as 70% at [Fe/H] < −3.0. Recall that, at present, we have not applied corrections to the photometric [C/Fe] estimates arising from evolutionary effects. Even so, the observed trend is consistent with that found from high-resolution spectroscopy (Placco et al. 2014). It is notable that our sample contains over 120,000 CEMP stars (100,800 dwarfs and 15,000 giants), which is a lower limit due to the lack of evolutionary corrections. Finally, the distributions of [Mg/Fe]–[Fe/H] and [α/Fe]–[Fe/H] are shown in Figure 20.

Table 2 summarizes the contents of our final parameter sample. From a series of well-established techniques in our previous studies (Papers I and II), the effective temperatures, distances, surface gravities, and ages are derived for all 4.3 million and 3.8 million stars in the parameter sample. The astrometric information (i.e., parallaxes, proper motions, and their uncertainties), taken from Gaia EDR3 (Gaia Collaboration et al. 2021), as well as the available radial velocities, from a number of sources, is also included. The sample will be made publicly available at doi:10.5281/zenodo.13160149. The applicable range and typical uncertainty of the derived parameters are summarized in Table 3. Note that, although we report elemental-abundance estimates in our J-PLUS parameter sample over a wide range, the quoted uncertainties only apply to the listed range. Outside of these ranges, the typical errors increase.

7. Summary and Future Prospects

In this paper, we determine stellar parameters (including effective temperature, surface gravity, [Fe/H], and age) and the important elemental-abundance ratios ([C/Fe], [Mg/Fe], and [α/Fe]) for over five million stars (4.5 million dwarf stars and

Table 2
Description of the Final Sample

Field	Description	Unit
Sourceid	Gaia EDR3 source ID	…
ra	R.A. from J-PLUS DR3 (J2000)	deg
dec	Decl. from J-PLUS DR3 (J2000)	deg
gl	Galactic longitude derived from ICRS coordinates	deg
gb	Galactic latitude derived from ICRS coordinates	deg
$mag_{1...12}$	Magnitudes of J-PLUS 12 bands	…
$err\_mag_{1...12}$	Uncertainties of magnitudes of J-PLUS 12 bands	mag
g/r/i	Magnitudes from Pan-STARRS1	…
err_g/r/i	Uncertainties of magnitudes from Pan-STARRS1	mag
G/BP/RP	Magnitudes for the three Gaia bands from EDR3; note G represents a calibration-corrected G magnitude	…
err_G/BP/RP	Uncertainties of magnitudes for the three Gaia bands from EDR3	mag
ebv_sfd	Value of $E(B-V)$ from the extinction map of SFD, corrected for a 14% systematic	…
[Fe/H]	Photometric metallicity	…
err_[Fe/H]	Uncertainty of photometric metallicity	dex
flg_[Fe/H]	Quality flag of [Fe/H]	…
[C/Fe]	Photometric carbon-to-iron abundance ratio	…
err_[C/Fe]	Uncertainty of photometric carbon-to-iron abundance ratio	dex
flg_[C/Fe]	Quality flag of [C/Fe]	
[Mg/Fe]	Photometric magnesium-to-iron abundance ratio	…
err_[Mg/Fe]	Uncertainty of photometric magnesium-to-iron abundance ratio	dex
flg_[Mg/Fe]	Quality flag of [Mg/Fe]	…
[α/Fe]	Photometric alpha-to-iron abundance ratio	…
err_[α/Fe]	Uncertainty of photometric alpha-to-iron abundance ratio	dex
flg_[α/Fe]	Quality flag of [α/Fe]	…
$T_{\rm eff}$	Effective temperature	K
err_$T_{\rm eff}$	Uncertainty of effective temperature	K
log g	Surface gravity	…
err_log g	Uncertainty of surface gravity	dex
dist	Distance	pc
err_dist	Uncertainty of distance	pc
flg_dist	Flag to indicate the method used to derive distance, which takes the values "parallax," "CMF," and "NO"	…
age	Stellar age	Gyr
err_age	Uncertainty of stellar age	Gyr
rv	Radial velocity	km s^{-1}
err_rv	Uncertainty of radial velocity	km s^{-1}
flg_rv	Flag to indicate the source of radial velocity, which takes the values "GALAH," "APOGEE," "Gaia," "RAVE," "LAMOST," "SEGUE"	…
parallax	Parallax from Gaia EDR3	mas
err_parallax	Uncertainty of parallax from Gaia EDR3	mas
pmra	Proper motion in R.A. direction from Gaia EDR3	mas yr^{-1}
err_pmra	Uncertainty of proper motion in R.A. direction from Gaia EDR3	mas yr^{-1}
pmdec	Proper motion in decl. direction from Gaia EDR3	mas yr^{-1}
err_pmdec	Uncertainty of proper motion in decl. direction from Gaia EDR3	mas yr^{-1}
ruwe	Renormalised unit weight error from Gaia EDR3	…
type	Flag to indicate classifications of stars, which takes the values "dwarf" and "giant"	…
subtype	Flag to indicate further subclassifications of dwarf stars, which takes the values "TO," "MS," and "Binary"	…

0.5 million giant stars) using 13 colors from a combination of narrowband and medium-band filter photometry from J-PLUS DR3 and ultrawide-band photometry from Gaia EDR3. To obtain estimates of metallicity and the elemental-abundance ratios, we have constructed a large training set consisting of millions of spectroscopically targeted stars. The scales for the metallicity and elemental-abundance ratios are carefully calibrated to previous results from high-resolution spectroscopic studies. The typical uncertainty is 0.10–0.20 dex for [Fe/H] and [C/Fe] and 0.05 dex for [Mg/Fe] and [α/Fe] over much of the range in metallicity.

Due to use of the narrow/medium-band filters employed by J-PLUS for both [Fe/H] (J0395) and [C/Fe] (J0430), the degeneracy between metallicity and carbonicity is successfully broken in this study. This is of particular importance for the VMP stars, where large fractions of carbon-enhanced stars are found, which have confounded metallicity estimates in previous photometric surveys (e.g., SAGES, SMSS, and Pristine).

Our photometric determination of [Fe/H] is well estimated down to [Fe/H] ~ -4.0, with a precision of 0.40 dex for dwarfs and 0.25 dex for giant stars, with no significant offsets. This sample thus opens the window to studies of the changes in the MDF and the fractions of CEMP stars for various disk and halo stellar populations based on a large, relatively bias-free sample of stars. Similar to previous efforts in this series, effective temperatures from broadband colors and photometric-metallicity estimates, distances from either Gaia parallaxes or

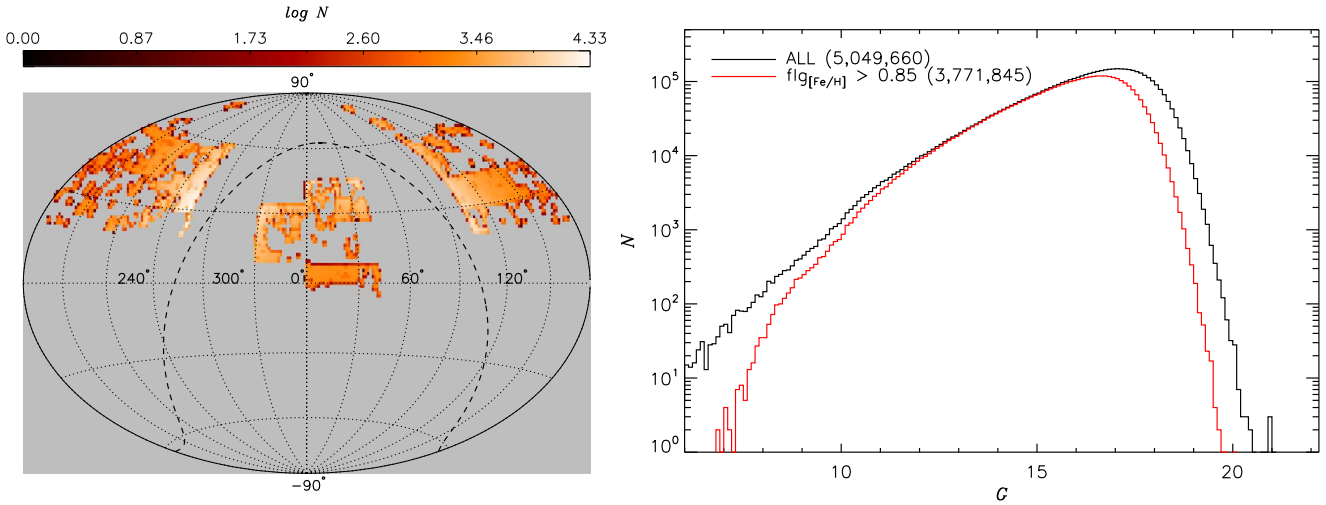

Figure 17. Left panel: density distribution of stars in the final J-PLUS parameter sample across the sky in equatorial coordinates. The black dashed line marks the Galactic plane. Right panel: magnitude distribution of stars in the final J-PLUS parameter sample in the Gaia G band. The red histogram represents the magnitude distribution for sample stars with $\mathtt{flg}_{[\mathrm{Fe/H}]} \geqslant 0.85$.

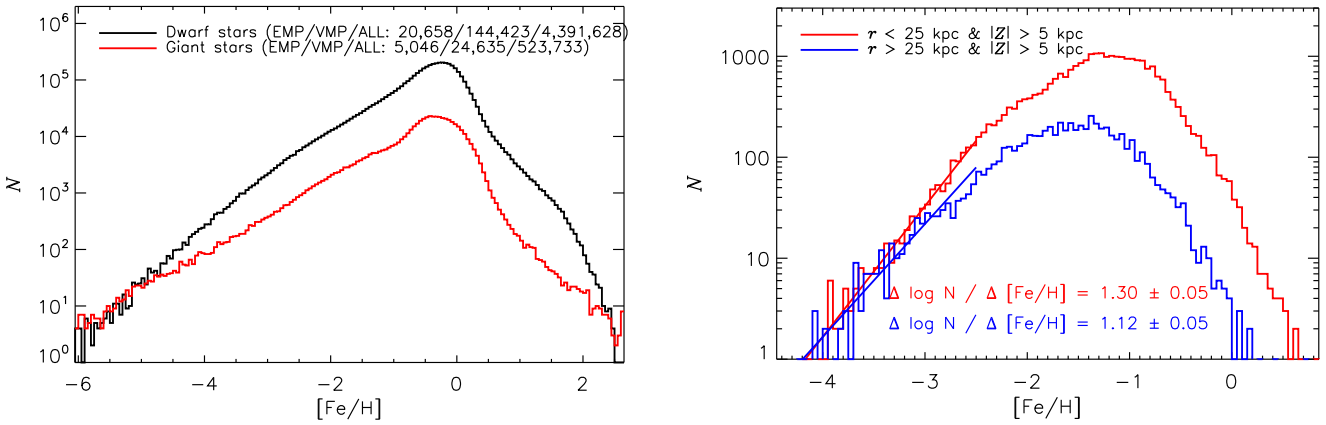

Figure 18. Left panel: the J-PLUS photometric-metallicity distributions for dwarfs (black histogram) and giant stars (red histogram). Right panel: the metallicity distribution functions of stars in the inner halo (red histogram; $r < 25$ kpc and $|Z| > 5$ kpc) and outer halo (blue histogram; $r > 25$ kpc and $|Z| > 5$ kpc) in the J-PLUS giant sample. The red and blue lines represent the best fits for their corresponding MDFs between [Fe/H] $= -2.75$ and -4.0, with the slopes listed at the bottom of the panel.

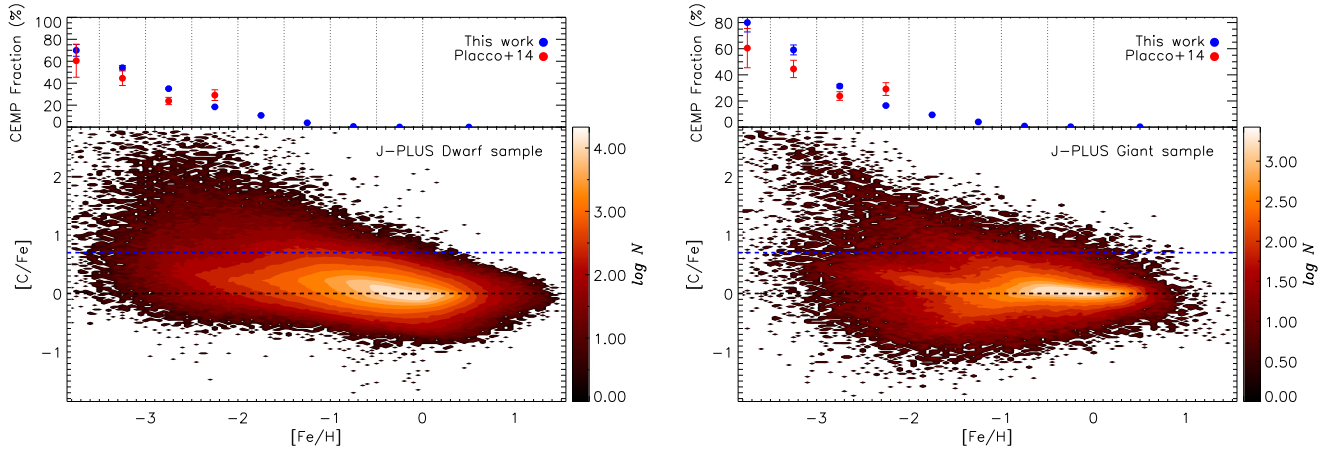

Figure 19. Left panel: density distribution of [C/Fe] vs. [Fe/H] for dwarf stars with $\mathrm{flg}_{[\mathrm{Fe/H}]} \geqslant 0.85$, $\mathrm{flg}_{[\mathrm{C/Fe}]} \geqslant 0.85$, and RUWE $\leqslant 1.4$, with a color bar shown on the right side. The black dashed and blue dashed lines represent [C/Fe] $= 0$ and [C/Fe] $= +0.7$, respectively. Stars with [Fe/H] $\leqslant -1.0$ and [C/Fe] $> +0.7$ are CEMP stars. The top subpanel plots the fraction of CEMP stars as a function of [Fe/H]. The red dots are the results taken from Placco et al. (2014). Right panel: similar to the left panel, but for giant stars. Note that, at present, we have not applied evolutionary corrections to the measured [C/Fe] in our sample.

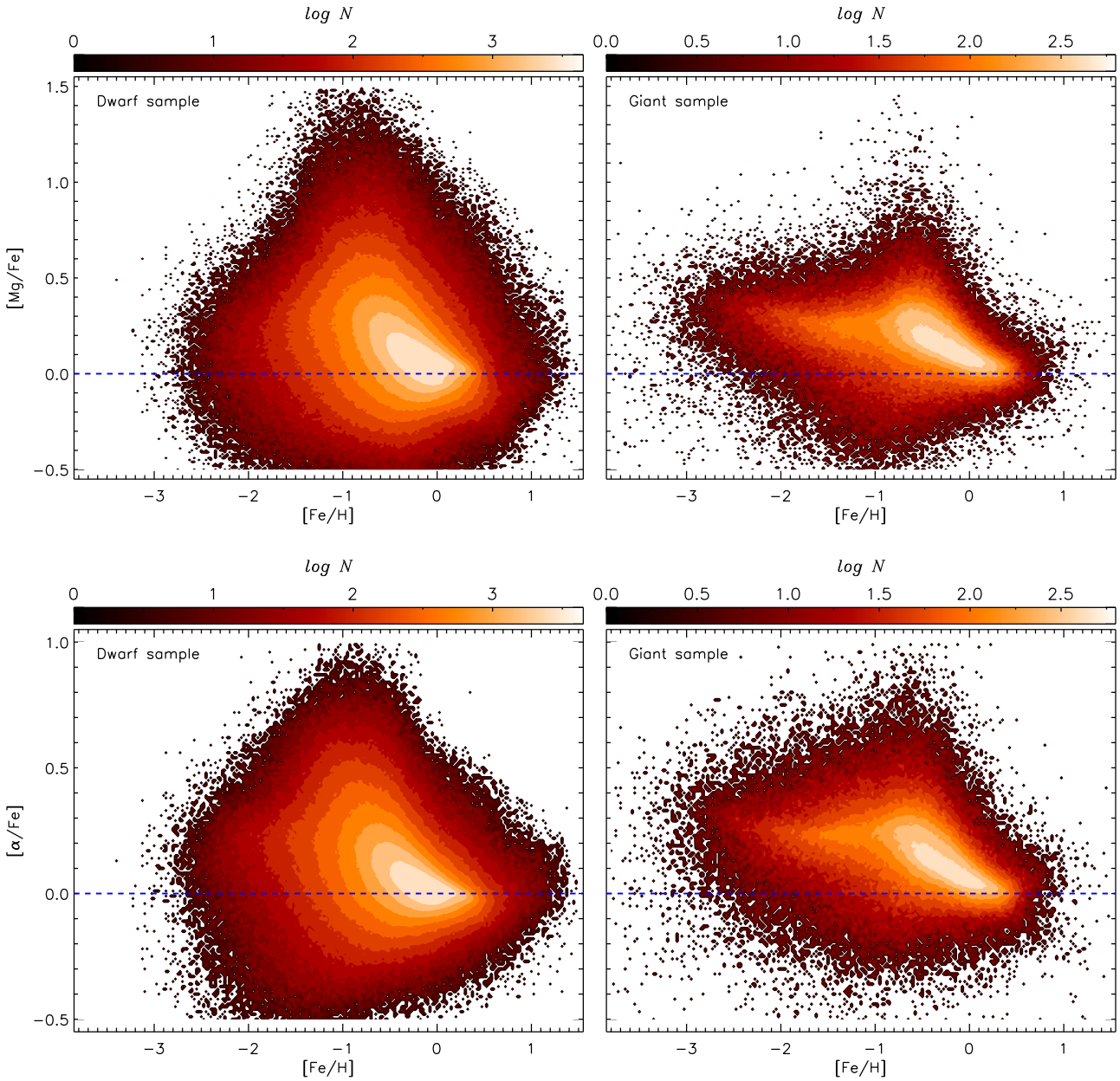

Figure 20. Upper panels: density distributions of [Mg/Fe] vs. [Fe/H] for dwarf (left) and giant (right) stars with $\mathrm{flg}_{[\mathrm{Fe/H}]} \geqslant 0.85$, $\mathrm{flg}_{[\mathrm{Mg/Fe}]} \geqslant 0.85$, and RUWE $\leqslant 1.4$, with a color bar shown on the top. Lower panels: similar to upper panels, but for [α/Fe] vs. [Fe/H]. The blue dashed lines in each panel indicate the solar ratios.

Table 3
The Applicable Range and Typical Uncertainty of Derived Parameters

Parameter	Luminosity Classification	Applicable Range	Typical Uncertainty
T_{eff}	Dwarf stars	[3800, 8000] K	100 K
	Giant stars	[3800, 6500] K	100 K
[Fe/H]	Dwarf stars	[−4.0, +1.0]	0.1 dex for [Fe/H] > −2.0 and 0.15–0.25 dex for [Fe/H] < −2.5
	Giant stars	[−4.0, +1.0]	0.1–0.2 dex for [Fe/H] > −2.0 and 0.2–0.4 dex for [Fe/H] < −1.0
[C/Fe]	Dwarf stars	[−1.5, +4.0]	0.1–0.2 dex
	Giant stars	[−1.5, +4.0]	0.1–0.2 dex
[Mg/Fe]	Dwarf stars	[−0.3, +0.6]	0.1–0.2 dex
	Giant stars	[−0.3, +0.6]	0.1–0.2 dex
[α/Fe]	Dwarf stars	[−0.2, +0.5]	0.03–0.06 dex
	Giant stars	[−0.2, +0.5]	0.02–0.05 dex
Age	⋯	Turnoff, main sequence, and subgiant stars	20%
log$g$	⋯	[0.0, 5.0]	0.1–0.2 dex

metallicity-dependent color–absolute magnitude fiducials, and ages from isochrone comparisons are included in the final parameter catalog.

The J-PLUS effort is still underway, and will at least double the numbers of stars in the northern sky for which we can determine precise metallicity and elemental-abundance estimates once it is completed in the next few years. The Southern Photometric Local Universe Survey (S-PLUS; Mendes de Oliveira et al. 2019) is a parallel survey of the southern sky (using an identical telescope and filter set to J-PLUS), for which we will report results from a similar analysis for the stars in its soon-to-be publicly released DR4 (Herpich et al. 2024) in the next paper in this series (Y. Huang et al. 2024, in preparation). We are also currently extending our techniques to include estimates of the [N/Fe] and [Ca/Fe] abundance ratios based on other narrow/medium-band filters employed by both J-PLUS and S-PLUS.

We can expect tens of millions of stars with precise elemental-abundance estimates once both surveys are completed, including stars in the disk and halo populations, in the direction of the Galactic Bulge, for stars associated with stellar streams, and for nearby canonical dwarf spheroidal galaxies and ultrafaint dwarf galaxies. One obvious application will be the construction of "blueprints" of Galactic stellar populations following the methods described in the series of papers by An & Beers (2020, 2021a, 2021b) and An et al. (2023). Other applications include analysis of the chemodynamical nature of stars in the disk and halo systems of the MW, such as the identification of dynamically and chemodynamically tagged groups, and their associations with recognized substructures (e.g., Shank et al. 2023; Zepeda et al. 2023; Cabrera Garcia et al. 2024, and references therein), and the identification of candidate very and extremely metal-poor stars in the disk system (e.g., Hong et al. 2024, and references therein). Clearly, our catalogs will also prove useful for identifying stars of particular interest for medium- and high-resolution spectroscopic follow-up studies.

Acknowledgments

We would like to thank the referee for helpful comments. Y.H. thanks Prof. H. W. Zhang and H. L. Chen for useful discussions on the uncertainties of [Fe/H] and elemental-abundance ratios in this work. This work is supported by the National Key R & D Program of China, grant No. 2019YFA0405500, and the National Natural Science Foundation of China, grant Nos. 12422303, 11903027, 11973001, 11833006, and 12222301. T.C.B. and J.H. acknowledge partial support from grant PHY 14-30152; Physics Frontier Center/JINA Center for the Evolution of the Elements (JINA-CEE), and from OISE-1927130: The International Research Network for Nuclear Astrophysics (IReNA), awarded by the US National Science Foundation. Y.S.L. acknowledges support from the National Research Foundation (NRF) of Korea grant funded by the Ministry of Science and ICT (NRF-2021R1A2C1008679 and RS-2024-00333766). Y.S.L. also gratefully acknowledges partial support for his visit to the University of Notre Dame from OISE-1927130: The International Research Network for Nuclear Astrophysics (IReNA), awarded by the US National Science Foundation. P.C. (Paul Coelho) acknowledges support from Conselho Nacional de Desenvolvimento Científico e Tecnológico (CNPq) under grant 310555/2021-3 and from Fundação de Amparoà Pesquisa do Estado de São Paulo (FAPESP) process number 2021/08813-7. S.D. acknowledges CNPq/MCTI for grant 306859/2022-0. P.C. (Patricia Cruz) and F.J.E acknowledge financial support from MCIN/AEI/10.13039/501100011033/ through grant PID2020-112949GB-I00. C.H.-M. acknowledges the support from the Spanish Ministry of Science and Education via project PID2021-126616NB-I00. A.E. acknowledges the financial support from the Spanish Ministry of Science and Innovation and the European Union—NextGenerationEU through the Recovery and Resilience Facility project ICTS-MRR-2021-03-CEFCA. L.S.J. acknowledges the support from CNPq (308994/2021-3) and FAPESP (2011/51680-6).

Based on observations made with the JAST80 telescope at the Observatorio Astrofísico de Javalambre (OAJ), in Teruel, owned, managed, and operated by the Centro de Estudios de Física del Cosmos de Aragón. We acknowledge the OAJ Data Processing and Archiving Department (DPAD) for reducing and calibrating the OAJ data used in this work, as well as the distribution of the data products through a dedicated web portal. Funding for the J-PLUS Project has been provided by the Governments of Spain and Aragón through the Fondo de Inversiones de Teruel; the Aragonese Government through the Research Groups E96, E103, E16_17R, E16_20R, and E16_23R; the Spanish Ministry of Science and Innovation (MCIN/AEI/10.13039/501100011033 y FEDER, Una manera de hacer Europa) with grants PID2021-124918NB-C41, PID2021-124918NB-C42, PID2021-124918NA-C43, and PID2021-124918NB-C44; the Spanish Ministry of Science, Innovation and Universities (MCIU/AEI/FEDER, UE) with grants PGC2018-097585-B-C21 and PGC2018-097585-B-C22; the Spanish Ministry of Economy and Competitiveness (MINECO) under AYA2015-66211-C2-1-P, AYA2015-66211-C2-2, AYA2012-30789, and ICTS-2009-14; and European FEDER funding (FCDD10-4E-867, FCDD13-4E-2685). The Brazilian agencies FINEP, FAPESP, and the National Observatory of Brazil have also contributed to this project.

The Guoshoujing Telescope (the Large Sky Area Multi-Object Fiber Spectroscopic Telescope, LAMOST) is a National Major Scientific Project built by the Chinese Academy of Sciences. Funding for the project has been provided by the National Development and Reform Commission. LAMOST is operated and managed by the National Astronomical Observatories, Chinese Academy of Sciences.

Appendix A
Calibrations

The APOGEE DR17, GALAH+ DR3, and SDSS/SEGUE DR12 are cross-matched with the collected HRS sample (PASTEL+SAGA), and the stars in common are used to examine the metallicity scales of these spectroscopic surveys. The results are shown in Figure A1. Generally, the metallicity of the three surveys is consistent with that of the HRS sample, but deviates significantly toward the metal-poor region. To correct for these systematics, second- and third-order polynomial functions are applied. In Figure A2, we adjust the LAMOST DR9 [Fe/H] scale to that of APOGEE DR17, correcting for small systematic trends with $T_{\rm eff}$, $\log g$, and [Fe/H]. Finally, the comparisons in Figure A3 show that the metallicity scale of the LAMOST/SEGUE VMP samples is quite consistent with that of HRS. A summary of the calibrations is presented in Table A1.

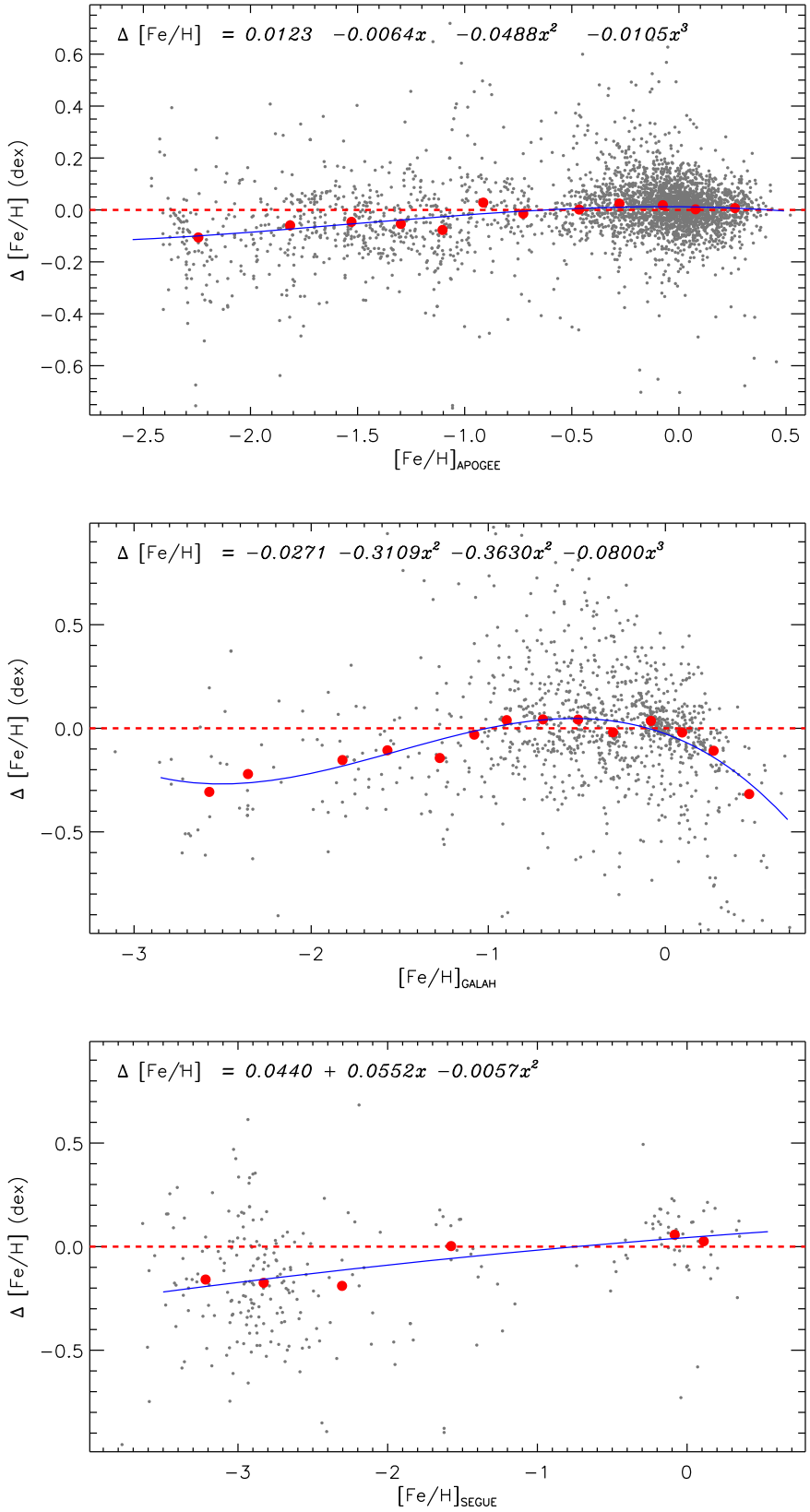

Figure A1. Metallicity differences (HRS minus APOGEE/GALAH/SDSS) between the stars in common between APOGEE (top panel), GALAH (middle panel), SDSS/SEGUE (bottom panel), and the HRS, as a function of [Fe/H]. The red dots in each panel represent the median of the metallicity differences in the individual metallicity bins. Blue lines (with the functions marked in the top left corner; here x is [Fe/H] of each spectroscopic survey) show second- to third-order polynomial fits to the blue data points. The red dashed lines indicate zero residuals in each panel.

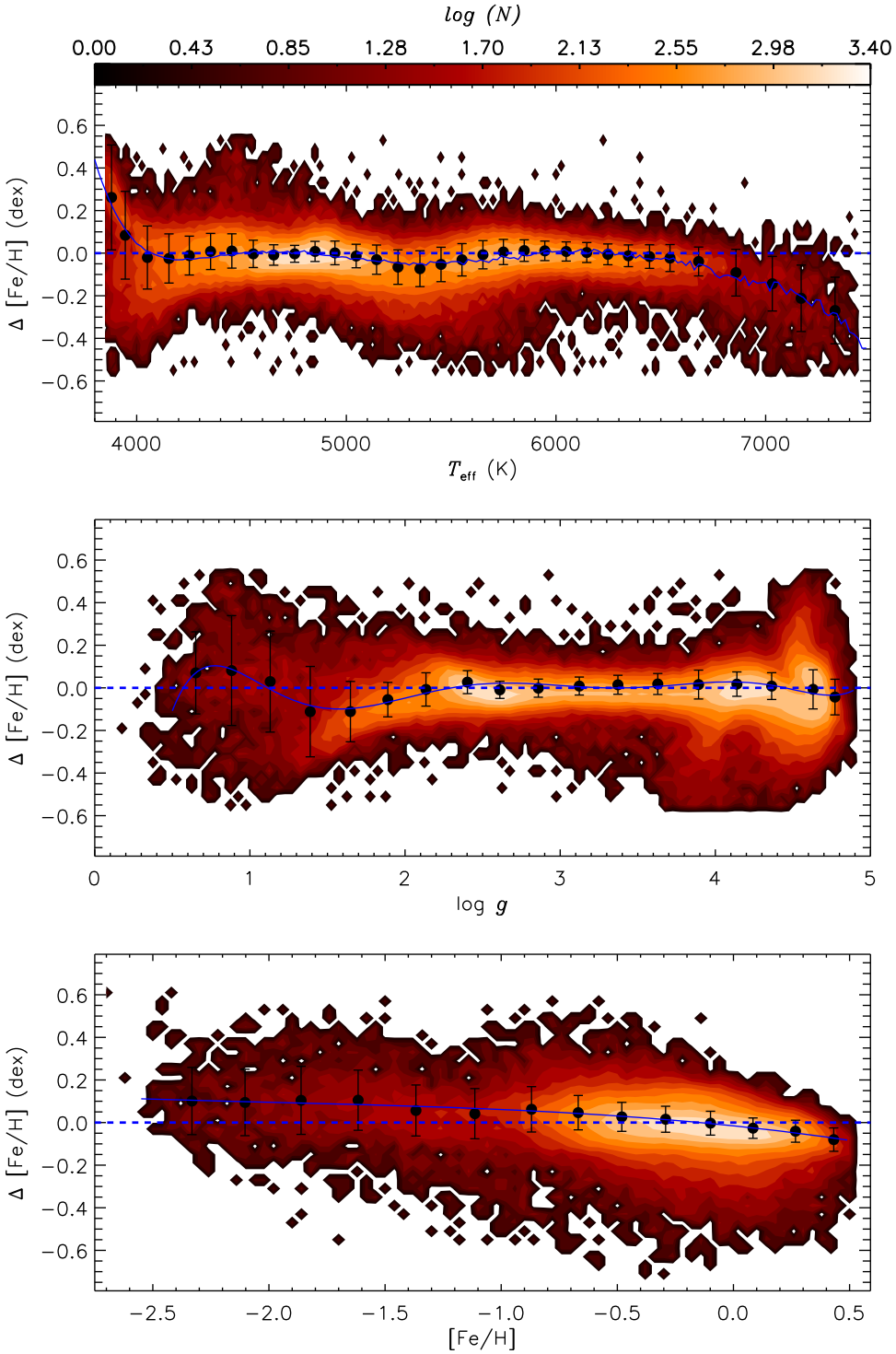

Figure A2. Density distributions of the metallicity differences (APOGEE minus LAMOST) as a function of LAMOST effective temperature (top panel), surface gravity (middle panel), and [Fe/H] (bottom panel). The black dots and error bars in each panel represent the median and dispersion of the metallicity differences in the individual parameter bins. Blue lines show third- and seventh-order polynomial fits to the black data points. The function in the top panel is $\Delta[\mathrm{Fe/H}] = 5.89680 \times 10^{3} - 7.50396 \times 10^{0} T_{\rm eff} + 4.05925 \times 10^{-3} T_{\rm eff}^{2} - 1.21006 \times 10^{-6} T_{\rm eff}^{3} + 2.14707 \times 10^{-10} T_{\rm eff}^{4} - 2.26794 \times 10^{-14} T_{\rm eff}^{5} + 1.32079 \times 10^{-18} T_{\rm eff}^{6} - 3.27244 \times 10^{-23} T_{\rm eff}^{7}$. The function in the middle panel is $\Delta[\mathrm{Fe/H}] = -3.49234 \times 10^{0} + 1.43439 \times 10^{1} \log g - 2.18911 \times 10^{1} \log g^{2} + 1.65358 \times 10^{1} \log g^{3} - 6.85637 \times 10^{0} \log g^{4} + 1.59063 \times 10^{0} \log g^{5} - 1.93735 \times 10^{-1} \log g^{6} + 9.64794 \times 10^{-3} \log g^{7}$. The function in the bottom panel is $\Delta[\mathrm{Fe/H}] = -1.54691 \times 10^{-2} - 1.12912 \times 10^{-1}[\mathrm{Fe/H}] - 4.32802 \times 10^{-2}[\mathrm{Fe/H}]^{2} - 7.26999 \times 10^{-3}[\mathrm{Fe/H}]^{3}$. A color bar representing the numbers of stars is provided above the top panel. The blue dashed lines indicate zero residuals in each panel.

For [C/Fe], [Mg/Fe], and [α/Fe], the scales of APOGEE DR17 are adopted as the reference ones. The elemental-abundance ratios derived from GALAH DR3 and LAMOST/SEGUE VMP samples are examined with APOGEE DR17 (see Figures A4 and A5). The results are summarized in Tables A2–A4. We note that no correlations are found for [C/Fe] between APOGEE DR17 and GALAH DR3. Therefore, no calibrations are performed for GALAH DR3.

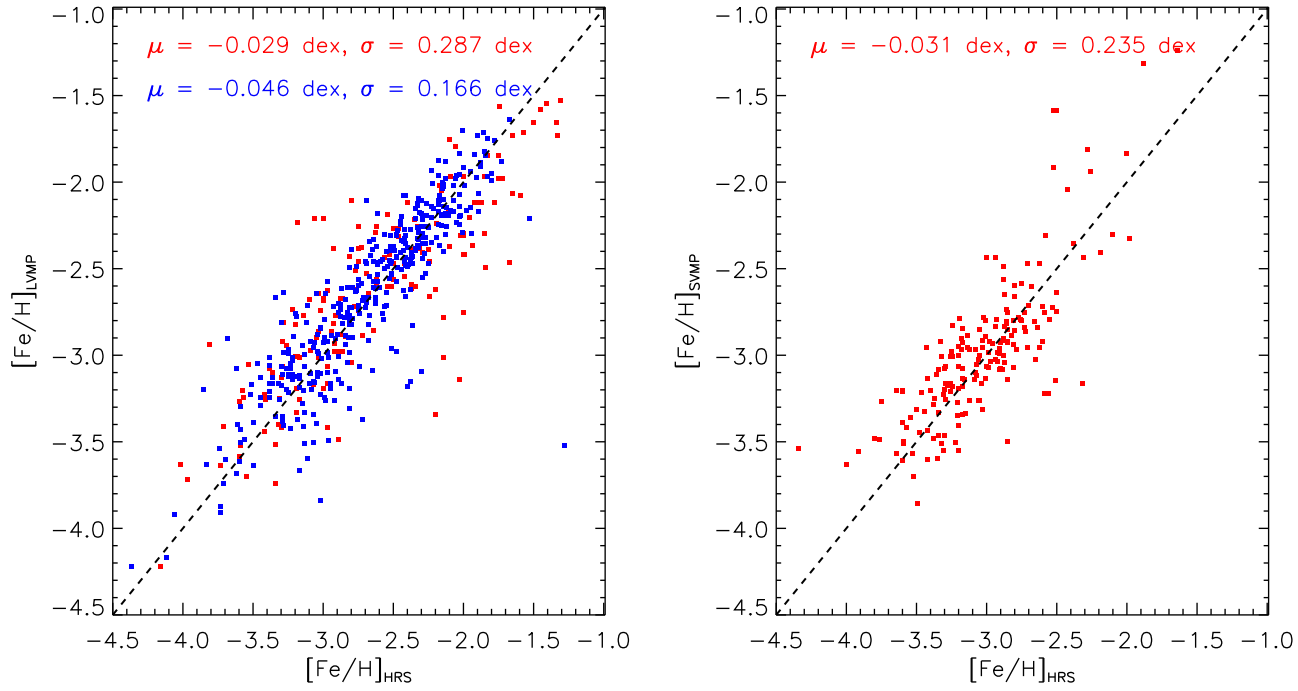

Figure A3. Left panel: comparisons between the LAMOST VMP (LVMP for short) sample (derived with the LSSPP; see Section 3.1 for details) and the HRS sample compiled from PASTEL+SAGA (red squares), and the LAMOST-Subaru HRS sample (blue squares) from Li et al. (2022). The overall median offset and standard deviation are marked in the top left corner. Right panel: comparison between the SDSS/SEGUE VMP (SVMP for short) sample (derived from the SSPP) and the HRS sample compiled from PASTEL+SAGA. The black dashed lines are the one-to-one lines.

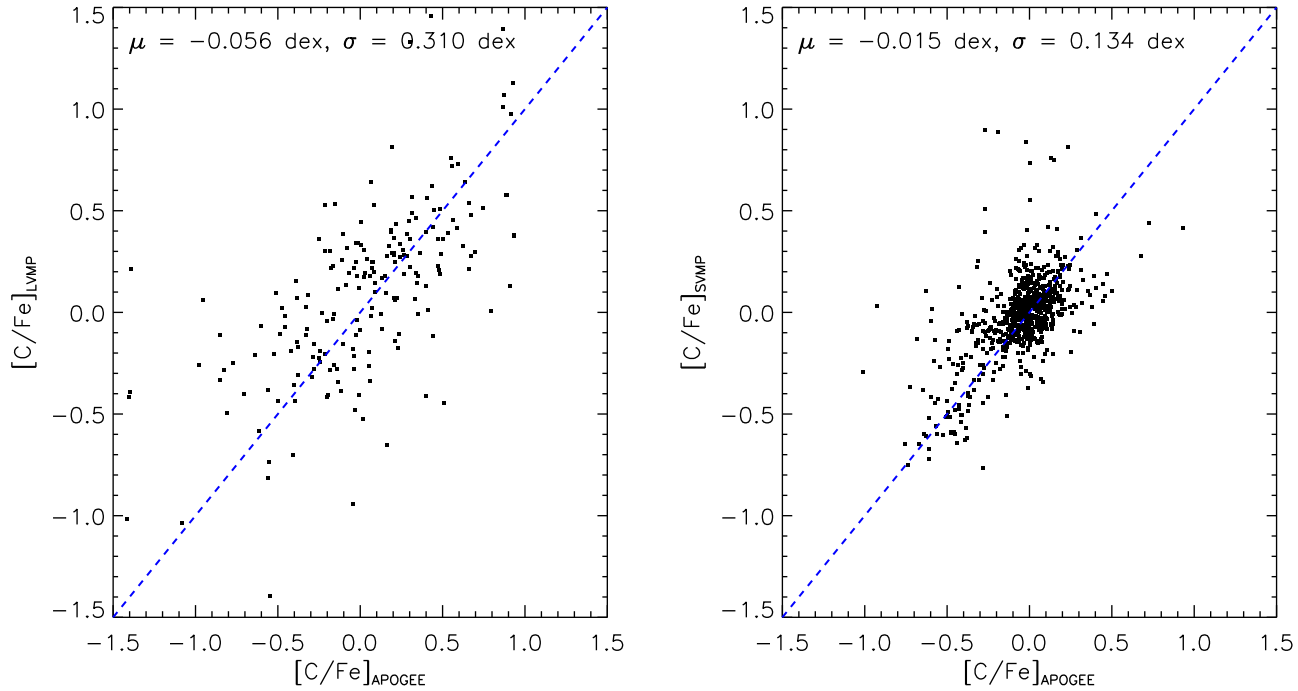

Figure A4. Comparisons between [C/Fe] from the LAMOST VMP (LVMP for short) sample (left panel) and the SDSS/SEGUE VMP (SVMP for short) sample (right panel) and that of APOGEE DR17 for stars (requiring spectral SNR greater than 50 pixel^{-1} in each survey) in common. The overall median offset and standard deviation are marked in the top left corner of each panel.

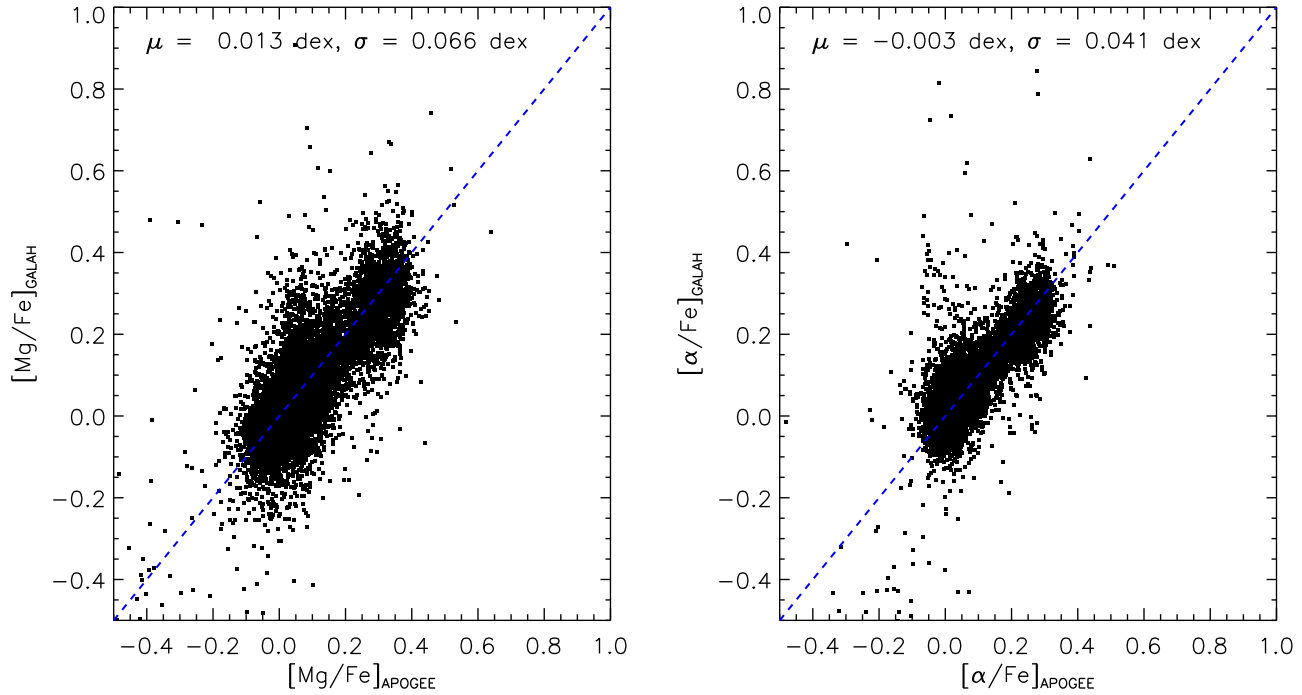

Figure A5. Comparisons between [Mg/Fe] (left panel) and [α/Fe] (right panel) of GALAH DR3 and those of APOGEE DR17. The overall median offset and standard deviation are marked in the top left corner or each panel. Note that the spectral SNR of the stars in common is required to be greater than 50 pixel^{-1} in each survey.

Table A1
Summary of the Training and Testing Samples for Metallicity ([Fe/H])

Catalog	N[a]	Metallicity Range	σ_1[b] (dex)	σ_2[c] (dex)	Calibration Note
PASTEL+SAGA	24,160	[−5.70, +1.00]	⋯	⋯	Reference scale
APOGEE DR17	642,616	[−2.47, +0.70]	0.075	0.073	Calibrated to the reference scale
GALAH DR3	438,397	[−4.53, +1.00]	0.172	0.162	Calibrated to the reference scale
LAMOST DR9	4,755,823	[−2.50, +1.00]	0.053	0.047	Calibrated to the scale of APOGEE DR17[d]
SDSS DR12	385,326	[−4.50, +0.75]	0.258	0.213	Calibrated to the reference scale
LAMOST VMP	42,221	[−4.78, −1.80]	0.287	⋯	No corrections
SDSS VMP	163,525	[−4.41, −0.80]	0.237	⋯	No corrections

Notes.
[a] Here N is the number of unique stars in the catalog with spectral SNR greater than 10 pixel^{-1}.
[b] σ_1 represents the standard deviation of the metallicity difference between the specific catalog and the reference scale.
[c] σ_2 represents the standard deviation of the metallicity difference between the specific catalog with calibrations and the reference scale.
[d] After calibration with APOGEE DR17, the metallicity scale of LAMOST DR9 can be further tied to the reference scale using the relations found for APOGEE DR17.

Table A2
Summary of the Training and Testing Samples for [C/Fe]

Catalog	N[a]	[C/Fe] Range	μ (dex)	σ (dex)	Calibration Note
APOGEE DR17	642,616	[−2.05, +1.30]	⋯	⋯	Reference scale
LAMOST VMP	37,716	[−5.77, +4.41]	−0.056	0.310	No corrections
SDSS VMP	152,504	[−2.23, +4.14]	−0.015	0.134	No corrections

Note.
[a] Here N is the number of unique stars with [C/Fe] measured in the catalog with spectral SNR greater than 10 pixel^{-1}.

Table A3
Summary of the Training Samples for [Mg/Fe]

Catalog	N[a]	[Mg/Fe] Range	μ (dex)	σ (dex)	Calibration Note
APOGEE DR17	642,616	[−1.71, +1.87]	⋯	⋯	Reference scale
GALAH DR3	425,203	[−1.46, +1.50]	−0.003	0.041	No corrections
LAMOST VMP[b]	32,485	[−1.52, +2.63]	−0.008	0.171	No corrections
SDSS VMP	101,770	[−1.01, +2.66]	−0.144	0.096	Corrected

Notes.
[a] Here N is the number of unique stars with [Mg/Fe] measured in the catalog with spectral SNR greater than 10 pixel^{-1}.
[b] Here [α/Fe] measurements are used since there are no [Mg/Fe] measurements for the LAMOST VMP sample.

Table A4
Summary of the Training Samples for [α/Fe]

Catalog	N[a]	[α/Fe] Range	μ (dex)	σ (dex)	Calibration Note
APOGEE DR17	642,616	[−1.68, +1.70]	⋯	⋯	Reference scale
GALAH DR3	425,203	[−1.26, +2.81]	−0.003	0.041	No corrections
LAMOST VMP	32,485	[−1.52, +2.63]	−0.051	0.174	Corrected
SDSS VMP	101,770	[−1.01, +2.61]	−0.135	0.077	Corrected

Note.
[a] Here N is the number of unique stars with [α/Fe] measured in the catalog with spectral SNR greater than 10 pixel^{-1}.

ORCID iDs

Yang Huang (黄样) https://orcid.org/0000-0003-3250-2876
Timothy C. Beers https://orcid.org/0000-0003-4573-6233
Kai Xiao (肖凯) https://orcid.org/0000-0001-8424-1079
Haibo Yuan (苑海波) https://orcid.org/0000-0003-2471-2363
Young Sun Lee https://orcid.org/0000-0001-5297-4518
Hongrui Gu (顾弘睿) https://orcid.org/0009-0007-5610-6495
Jihye Hong https://orcid.org/0000-0002-2453-0853
Jifeng Liu (刘继峰) https://orcid.org/0000-0002-2874-2706
Zhou Fan (范舟) https://orcid.org/0000-0003-3067-3540
Paula Coelho https://orcid.org/0000-0003-1846-4826
Patricia Cruz https://orcid.org/0000-0003-1793-200X
F. J. Galindo-Guil https://orcid.org/0000-0003-4776-9098
Simone Daflon https://orcid.org/0000-0001-9205-2307
Fran Jiménez-Esteban https://orcid.org/0000-0002-6985-9476
Antonio Marín-Franch https://orcid.org/0000-0002-9026-3933
Héctor Vázquez Ramió https://orcid.org/0000-0003-3135-2191

References

Abdurro'uf, Accetta, K., Aerts, C., et al. 2022, ApJS, 259, 35
Alam, S., Albareti, F. D., Allende Prieto, C., et al. 2015, ApJS, 219, 12
An, D., & Beers, T. C. 2020, ApJ, 897, 39
An, D., & Beers, T. C. 2021a, ApJ, 907, 101
An, D., & Beers, T. C. 2021b, ApJ, 918, 74
An, D., Beers, T. C., Lee, Y. S., & Masseron, T. 2023, ApJ, 952, 66
Andrae, R., Rix, H.-W., & Chandra, V. 2023, ApJS, 267, 8
Aoki, W., Li, H., Matsuno, T., et al. 2022, ApJ, 931, 146
Bailer-Jones, C. A. L., Rybizki, J., Fouesneau, M., Demleitner, M., & Andrae, R. 2021, AJ, 161, 147
Bertin, E., & Arnouts, S. 1996, A&AS, 117, 393
Bowen, I. S., & Vaughan, A. H. J. 1973, ApOpt, 12, 1430
Bressan, A., Marigo, P., Girardi, L., et al. 2012, MNRAS, 427, 127
Buder, S., Sharma, S., Kos, J., et al. 2021, MNRAS, 506, 150
Cabrera Garcia, J., Beers, T. C., Huang, Y., et al. 2024, MNRAS, 527, 8973
Cenarro, A. J., Moles, M., Cristóbal-Hornillos, D., et al. 2019, A&A, 622, A176
Cenarro, A. J., Moles, M., Marín-Franch, A., et al. 2014, Proc. SPIE, 9149, 91491I
Cui, X.-Q., Zhao, Y.-H., Chu, Y.-Q., et al. 2012, RAA, 12, 1197
De Silva, G. M., Freeman, K. C., Bland-Hawthorn, J., et al. 2015, MNRAS, 449, 2604
Deng, L.-C., Newberg, H. J., Liu, C., et al. 2012, RAA, 12, 735
Ezzeddine, R., Rasmussen, K., Frebel, A., et al. 2020, ApJ, 898, 150
Fan, Z., Zhao, G., Wang, W., et al. 2023, ApJS, 268, 9
Gaia Collaboration, Brown, A. G. A., Vallenari, A., et al. 2021, A&A, 649, A1
Galarza, C. A., Daflon, S., Placco, V. M., et al. 2022, A&A, 657, A35
García Pérez, A. E., Allende Prieto, C., Holtzman, J. A., et al. 2016, AJ, 151, 144
Gilmore, G., Randich, S., Worley, C. C., et al. 2022, A&A, 666, A120
Gunn, J. E., Siegmund, W. A., Mannery, E. J., et al. 2006, AJ, 131, 2332
Hansen, T. T., Holmbeck, E. M., Beers, T. C., et al. 2018, ApJ, 858, 92
Herpich, F. R., Almeida-Fernandes, F., Oliveira Schwarz, G. B., et al. 2024, A&A, 689, A249
Holmbeck, E. M., Hansen, T. T., Beers, T. C., et al. 2020, ApJS, 249, 30
Hong, J., Beers, T. C., Lee, Y. S., et al. 2024, ApJS, 273, 12
Huang, Y., Beers, T. C., Wolf, C., et al. 2022, ApJ, 925, 164
Huang, Y., Beers, T. C., Yuan, H., et al. 2023, ApJ, 957, 65
Huang, Y., Liu, X.-W., Zhang, H.-W., et al. 2015, RAA, 15, 1240
Huang, Y., Schönrich, R., Zhang, H., et al. 2020, ApJS, 249, 29
Huang, Y., Yuan, H., Li, C., et al. 2021, ApJ, 907, 68
Lee, Y. S., Beers, T. C., Carlin, J. L., et al. 2015, AJ, 150, 187
Lee, Y. S., Beers, T. C., Sivarani, T., et al. 2008, AJ, 136, 2022
Li, H., Aoki, W., Matsuno, T., et al. 2022, ApJ, 931, 147
Li, X., Zhang, X., Xiong, S., Zheng, Y., & Li, H. 2023, MNRAS, 523, 5230
Limberg, G., Santucci, R. M., Rossi, S., et al. 2021, ApJ, 913, 11
López-Sanjuan, C., Vázquez Ramió, H., Xiao, K., et al. 2024, A&A, 683, A29
López-Sanjuan, C., Yuan, H., Vázquez Ramió, H., et al. 2021, A&A, 654, A61
Lucey, M., Al Kharusi, N., Hawkins, K., et al. 2023, MNRAS, 523, 4049
Luo, A. L., Zhao, Y.-H., Zhao, G., et al. 2015, RAA, 15, 1095
Majewski, S. R., Schiavon, R. P., Frinchaboy, P. M., et al. 2017, AJ, 154, 94
Marigo, P., Girardi, L., Bressan, A., et al. 2017, ApJ, 835, 77
Martin, N. F., Starkenburg, E., Yuan, Z., et al. 2023, arXiv:2308.01344
Mendes de Oliveira, C., Ribeiro, T., Schoenell, W., et al. 2019, MNRAS, 489, 241
Onken, C. A., Wolf, C., Bessell, M. S., et al. 2019, PASA, 36, e033
Placco, V. M., Frebel, A., Beers, T. C., & Stancliffe, R. J. 2014, ApJ, 797, 21

Placco, V. M., Santucci, R. M., Beers, T. C., et al. 2019, ApJ, 870, 122
Randich, S., Gilmore, G., Magrini, L., et al. 2022, A&A, 666, A121
Riello, M., D. Angeli, F., Evans, D. W., et al. 2021, A&A, 649, A3
Rockosi, C. M., Lee, Y. S., Morrison, H. L., et al. 2022, ApJS, 259, 60
Sakari, C. M., Placco, V. M., Farrell, E. M., et al. 2018, ApJ, 868, 110
Schlaufman, K. C., & Casey, A. R. 2014, ApJ, 797, 13
Schlegel, D. J., Finkbeiner, D. P., & Davis, M. 1998, ApJ, 500, 525
Schölkopf, B., Smola, A., & Müller, K.-R. 1998, Neural Computation, 10, 1299
Shank, D., Beers, T. C., Placco, V. M., et al. 2021, ApJ, 912, 147
Shank, D., Beers, T. C., Placco, V. M., et al. 2022, ApJ, 926, 26
Shank, D., Beers, T. C., Placco, V. M., et al. 2023, ApJ, 943, 23
Soubiran, C., Le Campion, J.-F., Brouillet, N., & Chemin, L. 2016, A&A, 591, A118
Starkenburg, E., Martin, N., Youakim, K., et al. 2017, MNRAS, 471, 2587
Steinmetz, M., Zwitter, T., Siebert, A., et al. 2006, AJ, 132, 1645
Suda, T., Katsuta, Y., Yamada, S., et al. 2008, PASJ, 60, 1159
Whitten, D. D., Placco, V. M., Beers, T. C., et al. 2019, A&A, 622, A182
Wolf, C., Onken, C. A., Luvaul, L. C., et al. 2018, PASA, 35, e010
Wu, Y., Xiang, M., Zhao, G., et al. 2019, MNRAS, 484, 5315
Xiang, M. S., Liu, X. W., Shi, J. R., et al. 2017, MNRAS, 464, 3657
Xiao, K., Huang, Y., Yuan, H., et al. 2024, ApJS, 271, 41
Xue, X.-X., Ma, Z., Rix, H.-W., et al. 2014, ApJ, 784, 170
Yang, L., Yuan, H., Xiang, M., et al. 2022, A&A, 659, A181
Yanny, B., Rockosi, C., Newberg, H. J., et al. 2009, AJ, 137, 4377
Yong, D., Da Costa, G. S., Bessell, M. S., et al. 2021, MNRAS, 507, 4102
York, D. G., Adelman, J., Anderson, J. E., Jr., et al. 2000, AJ, 120, 1579
Youakim, K., Starkenburg, E., Martin, N. F., et al. 2020, MNRAS, 492, 4986
Yuan, H. B., Liu, X. W., & Xiang, M. S. 2013, MNRAS, 430, 2188
Zepeda, J., Beers, T. C., Placco, V. M., et al. 2023, ApJ, 947, 23
Zhao, G., Zhao, Y.-H., Chu, Y.-Q., Jing, Y.-P., & Deng, L.-C. 2012, RAA, 12, 723